ChemComm

HIGHLIGHT

View Article Online
View Journal | View Issue

Check for updates

Cite this: *Chem. Commun.*, 2025, **61**, 14773

Advancing metal–organic frameworks and covalent organic frameworks for photocatalytic CO_2 reduction

Jeewon Bu, †[a] Woo Seok Cheon, †[a] Hyojung Kim, *[b] Myoung Hwan Oh*[c] and Ho Won Jang *[ad]

Increasing atmospheric carbon dioxide concentration necessitates innovative approaches to transform CO_2 into valuable compounds utilizing solar energy. The photocatalytic CO_2 reduction reaction (PC CRR) offers a sustainable solution, yet wide band gaps, rapid electron–hole recombination, and poor CO_2 adsorption capacity limit traditional metal oxide semiconductors for the PC CRR. This review systematically evaluates recent engineering advances in metal–organic frameworks (MOFs) and covalent organic frameworks (COFs) as efficient photocatalysts for the PC CRR. Their intrinsic porosity, structural versatility, and well-defined modular architectures facilitate enhanced light absorption, efficient charge separation, and improved CO_2 activation. Their electronic structures are easily regulated by ligand functionalization, metal substitution/introduction, and incorporating photosensitizers. Once they form a favorable heterojunction with other semiconductors, the interfacial electric field facilitates charge separation and transport, increasing the light utilization efficiency. MOFs can also be used as sacrificial templates to fabricate porous photocatalytic materials with enhanced light harvesting and high concentrations of active sites. After thoroughly discussing strategies for photocatalyst engineering, current challenges such as achieving more valuable hydrocarbons as reaction products are addressed, and future research directions are proposed.

Received 2nd July 2025,
Accepted 26th August 2025

DOI: 10.1039/d5cc03725e

rsc.li/chemcomm

---

[a] *Department of Materials Science and Engineering, Research Institute of Advanced Materials (RIAM), Seoul National University, Seoul, 08826, Republic of Korea. E-mail: hwjang@snu.ac.kr; Web: https://sites.google.com/view/onnl; Fax: +82-2-884-1413; Tel: +82-2-880-1720*

[b] *Department of Semiconductor Systems Engineering, Sejong University, Seoul, 05006, Republic of Korea*

[c] *Department of Energy Engineering, KENTECH Institute for Environmental and Climate Technology, Korea Institute of Energy Technology, Naju, 58330, Republic of Korea*

[d] *Advanced Institute of Convergence Technology, Seoul National University, Suwon, 16229, Republic of Korea*

† These authors contributed equally.

Jeewon Bu

Jeewon Bu is currently a PhD candidate under the supervision of Prof. Ho Won Jang in the Department of Materials Science and Engineering of Seoul National University. She received her BS degree from the Department of Physics, Ewha Womans University, in 2020. Her current research focuses on the design of metal–organic frameworks and their application in electrochemical water splitting.

Woo Seok Cheon

Woo Seok Cheon is currently a PhD candidate under the supervision of Prof. Ho Won Jang in the Department of Materials Science and Engineering of Seoul National University. He received his BS degree from the Department of Materials Science and Engineering of Seoul National University, in 2021. His current research focuses on the design of nanostructured metal-based electrocatalysts and their application in CO_2 reduction.

1. Introduction

Global warming and climate change are largely caused by the fast-rising concentration of carbon dioxide (CO_2) in the atmosphere, which results from increased industrial activity and the ongoing use of fossil fuels.[1] Various strategies are being researched to reduce carbon dioxide and achieve carbon neutrality, and among them, converting CO_2 into valuable chemical feedstocks and fuels using renewable energies is attracting attention. The photocatalytic CO_2 reduction reaction (PC CRR) has been discussed to be a candidate for an eco-friendly and sustainable solution.[2,3] The artificial photosynthetic process demonstrates several advantages over other approaches, such as mild reaction conditions, simple and scalable reactors, and direct utilization of limitless and unrestricted solar energy.[4] An effective PC CRR requires the development of photocatalytic materials with optimal band gaps for light harvesting, electronic structures for efficient charge separation and transfer, high concentration of active sites for CO_2 adsorption and activation.[5]

Initially, many researchers developed metal oxide-based photocatalysts such as TiO_2, ZnO, WO_3, and Ga_2O_3 due to their robustness, facile synthesis, and light absorption ability.[6–12] However, the large band gaps of metal oxides limit the range of absorbable light to ultraviolet (UV) rays (only ∼5% of solar energy),[13] and rich defects within their structure induce rapid charge recombination.[14] The lack of design versatility is also a drawback for the PC CRR. Since the CO_2 reduction reaction (CRR) is a multi-electron transfer reaction, the reaction pathway is complex and thus requires a catalytic site with well-designed chemical microenvironments to increase the selectivity of a specific product.[15,16]

Metal–organic frameworks (MOFs) and covalent organic frameworks (COFs) are emerging as innovative materials that are promising alternatives to conventional photocatalysts (Fig. 1a).[17] They offer superior properties like high CO_2 adsorption capacity, photosensitivity to visible light, high crystallinity and porosity, and structural diversity and tunability (Fig. 1b).[5,18] Molecular building blocks and their extensive connections constitute the reticular chemicals, enabling the fabrication of a modularly designed microenvironment.[19]

Hyojung Kim

Hyojung Kim is an Assistant Professor in the Department of Semiconductor Systems Engineering at Sejong University, Seoul, South Korea. She received her PhD in Materials Science and Engineering from Seoul National University in 2021, where she focused on halide perovskite-based resistive switching memory. Her research encompasses next-generation non-volatile memory, in-memory computing systems, photocatalysts, gas sensors, and spin valves. She is particularly interested in the structural and chemical mechanisms governing ion migration and redox processes in emerging memory devices.

Myoung Hwan Oh

Myoung Hwan Oh is an Associate Professor in the Department of Energy Engineering at the Korea Institute of Energy Technology (KENTECH). He earned his PhD in Chemical and Biological Engineering from Seoul National University, where he also completed his Bachelor's and Master's degrees. He worked as a postdoctoral researcher at the University of California, Berkeley, from 2014 to 2019, and later served as a Chemistry Scientist at the Joint Center for Artificial Photosynthesis at Lawrence Berkeley National Laboratory from 2019 to 2021. He then joined KENTECH, where his research focuses on designing advanced electrochemical materials through nanointerface and defect engineering, with applications in CO_2 and nitrate electrolysis, plasma catalysis, and gas sensing. His interests also extend to neuromorphic computing devices and LEDs, emphasizing the synthesis and self-assembly of nanocrystalline thin films, correlative microscopy, and machine learning-assisted characterization.

Ho Won Jang

Ho Won Jang is a full professor at the Department of Materials Science and Engineering, Seoul National University. He received his PhD degree from the Department of Materials Science and Engineering, Pohang University of Science and Technology in 2004. He worked as a research associate at the University of Madison-Wisconsin from 2006 to 2009. He worked at the Institute of Science and Technology of Korea as a senior research scientist before joining Seoul National University. His research interest includes the design of materials and device fabrication for (photo)electrocatalysis, thin film transistors, memristors, chemical sensors, and micro-light-emitting diodes.

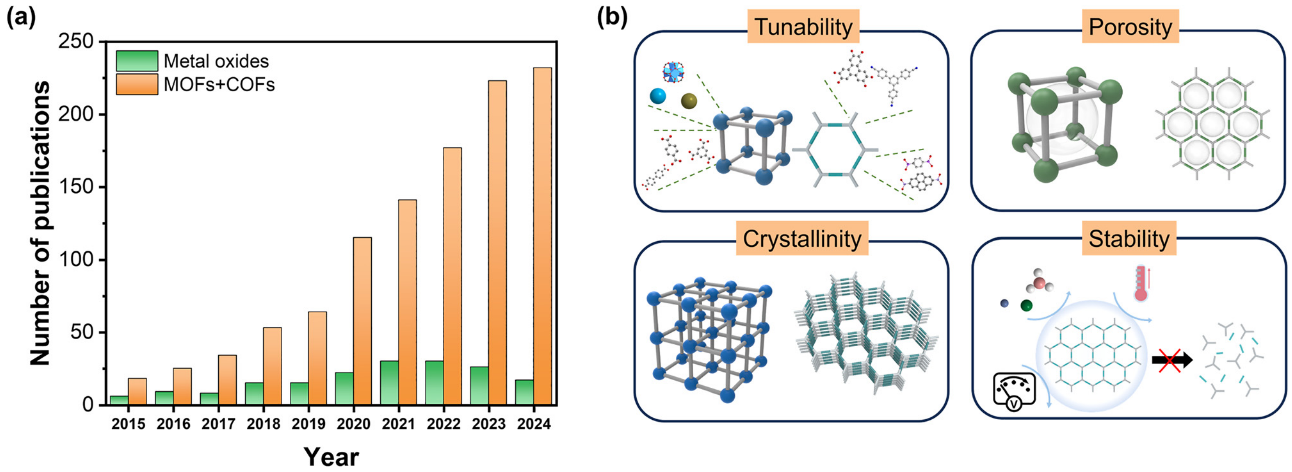

Fig. 1 (a) The annual number of publications for photocatalytic CO_2 reduction. (Keywords: "photocatalytic", "CO_2 reduction", "oxide", "MOF", "COF", "metal–organic framework", and "covalent organic frameworks". Data from Web of Science, June 2025). (b) Characteristics of MOFs and COFs in terms of key factors affecting photocatalytic performance.

MOFs are composed of metal nodes and organic ligands, while COFs are composed of organic building blocks with π-conjugated systems. The structural diversity and tunability allow for modulating the band gap, facilitating charge transfer, and enhancing catalytic activity. For example, changing the linkage between the Pd-complex and the azobenzene in the COF backbone from a simple coordination bond to cyclopalladation can significantly increase the absorption in the near-infrared region.[20] Additionally, their high porosity and large surface area maximize the exposure of active sites and mass transport of reactants. Both MOFs and COFs exhibit high crystallinity, which reduces charge recombination and promotes efficient charge separation and transport.[21] MOFs can host atomically dispersed active sites that show high selectivity for the CRR over competing side reactions.[22] Engineering the coordination of metal nodes and organic linkers modulates the electronic structure to improve light absorption.[23–25] COFs possess strong covalent bonding, which provides superior thermal and chemical stability, ensuring the retention of structural integrity over prolonged catalytic cycles.[21,26] Moreover, MOFs and COFs can be combined with other materials (such as semiconductors, photosensitizers, single atoms, *etc.*) or can be precursors of derivatives to improve their electrical conductivity and photocatalytic activity. Integration of the crystalline porous materials with semiconductors endows a favorable heterojunction for photo-generated charge carrier separation and transport. Metal chalcogenide nanoparticles or organic semiconductors such as g-C_3N_4 have been researched to enhance electron transfer to redox sites and obtain a higher quantum yield.[27–30]

When the reticular chemicals are utilized as precursors for nanomaterial fabrication, the derivatives maintain some characteristics, such as the porosity and morphology of the parent materials.[31] Post-synthetic treatment, including oxidation of MOFs, results in porous structures with a wider absorption range and enhanced chemical stability.[32–34]

As the interest in the synthesis and photocatalytic application of materials based on reticular chemistry continues to grow, a comprehensive review of such materials is required. It is time for a review that summarizes the recent developments and achievements of MOFs and COFs, focusing on CO_2 reduction, which can contribute the most to carbon neutrality among the many reactions that can occur under sunlight. This review aims to provide an in-depth analysis of the photocatalytic properties of MOF and COF-based photocatalysts, systematically summarizing strategies for enhancing their performance. First, principles of the PC CRR and design strategies will be introduced in several aspects such as light harvesting, charge separation and transport and catalytic activity. Afterward, pristine and functionalized MOFs and COFs, their composites and the derivatives will be discussed with selected examples. This work seeks to offer insights into the future development of MOF and COF-based materials and to outline key directions for the design of next-generation photocatalysts for CO_2 reduction.

2. Principles and design strategies of photocatalysts for CO_2 reduction

The PC CRR is a process that utilizes solar energy to convert CO_2 into valuable chemical products, following a principle similar to artificial photosynthesis. In MOF- and COF-based photocatalytic systems, the PC CRR proceeds through three key steps. First, the photocatalyst absorbs solar energy, then electrons excite from the highest occupied molecular orbital (HOMO) to the lowest unoccupied molecular orbital (LUMO).[31,35,36] The energy difference between these orbitals plays a crucial role in determining the feasibility of the CRR.[5,26,31,36] Second, the photogenerated electrons and holes migrate within the photocatalyst toward the reactive sites. However, during this process, charge recombination can frequently occur, reducing the overall efficiency of the reaction.[37] Third, electrons interact with the adsorbed CO_2, initiating a reduction process. The type of reduction products depends on the number of electrons transferred, with key products including carbon monoxide (CO), formic acid (HCOOH), formaldehyde (HCHO), methanol (CH_3OH), and methane (CH_4).[35,38]

Based on the understanding of the principles of the PC CRR, the following properties can be modified in MOF- and COF-based materials to improve their performance: CO_2 adsorption and activation, light absorption capacity, charge separation and transport efficiency, and the catalytic activity at redox centers.[5,37] These frameworks can function as light-harvesting units, redox-active centers, or host matrices for functionalized units, often fulfilling multiple roles simultaneously. Accordingly, the strategy for performance improvement is closely linked to the specific function for which the material is employed, as illustrated in Fig. 2.

The ability to absorb light is one of the most important characteristics that a photocatalyst must possess. Conventional metal oxide semiconductors typically absorb light in the UV spectrum, which limits the efficiency of catalytic reactions using sunlight. Therefore, if the light absorption spectrum of the photocatalyst is extended to the visible light range, solar energy can be utilized more effectively. The width of the band gap is a primary factor that dictates the light absorption range. A narrow band gap allows the absorption of a wide range of light, enhancing the generation and mobility of photoinduced charges; yet, it also elevates the possibility of electron recombination. For effective performance of the CRR, the energy gap between the HOMO and LUMO must be appropriately adjusted.[39] The LUMO level must be more negative than the reduction potential of CO_2. In contrast, the HOMO level should be more positive than the oxidation potential of the water oxidation reaction or other counter reactions.[39,40] MOFs and COFs have structural diversity, allowing various design strategies to tailor their electronic and optical properties. Selecting appropriate metal centers and organic linkers adjusts the electronic properties, and incorporating π-conjugated systems or donor–acceptor motifs enhances light absorption and charge transfer.[41] For instance, Fe–O clusters can absorb light and directly excite electrons to enable CO_2 reduction.[42] Likewise, porphyrin-based linkers exhibit significant light absorbance in the visible spectrum and efficiently generate charge carriers

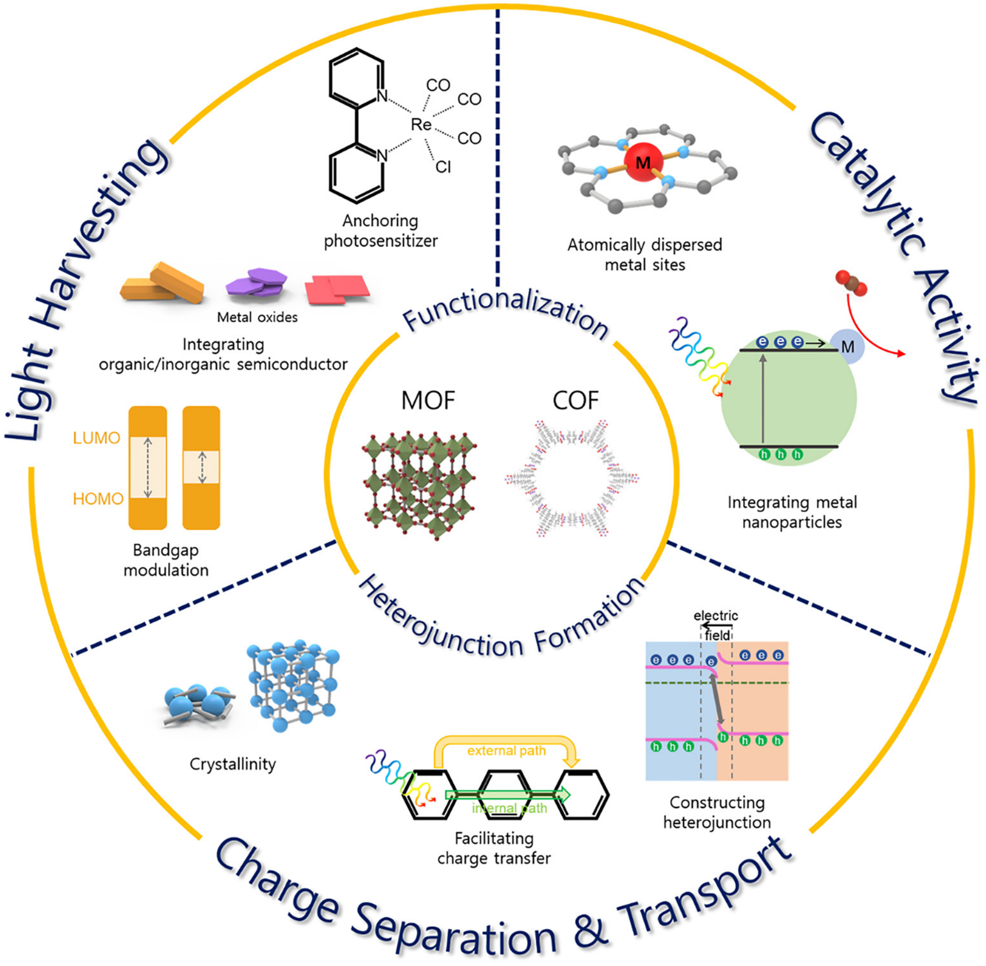

Fig. 2 Schematic illustration of strategies for photocatalysts based on MOFs and COFs for CO_2 reduction reaction.

upon light excitation.[43–46] Moreover, a high CO_2 adsorption capacity can be expected due to the strong interaction between porphyrin-based linkers and CO_2. However, porphyrin-based linkers may suffer from photooxidative degradation under aerobic conditions. Modifying ligand and metal nodes can effectively improve light absorption and optimize bandgap alignment.[47] Linker functionalization contributes to improving light absorption ability, thereby enabling more efficient utilization of visible light. In particular, the amine group acts as a light-absorbing antenna, increasing the light absorption range into visible light. Also, the amine group functions as an electron donor, enhancing catalytic activity and promoting electron transfer. Fu and coworkers demonstrated this by introducing an amine-functionalized organic ligand (BDC-NH_2) into MIL-125(Ti), forming NH_2-MIL-125(Ti).[48] Before the functionalization, light absorption mainly occurred in the UV spectrum. However, following the incorporation of the amine functional group, absorption within the visible light spectrum became feasible. Light absorption capability can be enhanced by strategically tuning the organic linker and metal cluster, while simultaneously improving CO_2 adsorption and charge transfer efficiency. For catalysts exhibiting insufficient light absorption, they can act as photocatalysts by combining with semiconductors (*i.e.* photosensitizers, metal oxides, *etc.*). Introducing a photosensitizer into MOFs and COFs can increase light absorption ability and optimize electron transfer. Bandgap engineering strategies will later be exemplified in Section 3.1 for MOFs with functionalized linkers and in Section 4.1 for COFs with extended π-systems.

To achieve effective CO_2 reduction, the photoinduced electrons must be efficiently transferred to the catalyst surface, while charge recombination must be minimized during this process. MOFs and COFs have high porosity and crystallinity, which promote charge transfer and suppress charge recombination. In MOFs, discrete metal clusters are periodically connected by organic linkers to construct a three-dimensional network, resulting in short electron hopping distances between adjacent metal nodes.[49] This framework architecture facilitates rapid photoinduced electron migration *via* site-to-site hopping, thereby decreasing electron–hole recombination probability.[50] By contrast, COFs possess extended π-conjugated networks within two-dimensional layers, supporting the delocalization of charge carriers throughout the covalently bonded planes.[51] Such continuous π-conjugation enables higher in-plane charge mobility than many 3D MOFs and suppresses carrier recombination by minimizing carrier localization. This delocalization reduces carrier localization and can sustain higher photocurrent densities. However, MOFs can offer shorten inter-node electron hopping distances in 3D space, which may benefit isotropic charge transport in bulk powders.

Furthermore, the charge transfer properties of MOFs and COFs are also influenced by their morphology. The regulation of crystallinity and bond polarization can improve carrier mobility.[21,52] The crystal size and arrangement of MOFs, as well as the stack arrangement of COFs, control the electron mobility path, which directly impacts the catalytic performance. For example, Song *et al.* synthesized two MOFs (Ni-MOF and Ni-MOF(H_2O)) with different crystal structures using the same linker and metal but with different synthesis methods.[53] Ni-MOF(H_2O) has a rhombus-shaped plate morphology while the Ni-MOF has a flexible nanosheet morphology. The Ni–C bond length of Ni-MOF(H_2O) has been determined to be 1.87 Å, shorter than that of the Ni-MOF of 1.95 Å, enhancing the electronic interaction with CO_2 and facilitating effective electron transport. As a result, Ni-MOF(H_2O) exhibited a better CO generation rate and selectivity than the Ni-MOF. Additionally, the integration of MOFs and COFs with metal oxides such as TiO_2, Cu_2O, WO_3, *etc.* to create a type-II or Z-scheme heterojunction results in the spatial separation of electrons and holes, thereby inhibiting recombination and enhancing charge transfer efficiency.[54] The presence of an internal electric field within heterostructures further enhances charge carrier separation. A Z-scheme heterojunction consists of two or more semiconductors in which electrons from one component recombine with holes from another. Compared with simple type-II junctions, Z-scheme configurations can better preserve strong redox potentials on both components, albeit often at the cost of increased recombination loss at the mediator interface.[55] The choice between these architectures should therefore balance redox driving force and recombination risk in the intended reaction pathway.[56] Wang *et al.* maximized the CO_2 photoreduction performance by combining TiO_2 and Cu(II) porphyrin-functionalized UiO-66 MOFs to form a MOF-semiconductor heterojunction.[57] Photocurrent analysis and electrochemical impedance analysis demonstrated that the heterojunction formation between MOFs and TiO_2 was a key factor in promoting electron transfer and enhancing catalytic reactivity. Besides semiconductors, the integration with diverse materials such as quantum dots (QDs), g-C_3N_4, and single atoms can yield a high-performance catalyst that leverages the benefits of MOFs and COFs while addressing their limitations. In Sections 3.2 and 4.2, MOF/COF-semiconductor heterojunctions demonstrate how band alignment at the interface improves charge separation, or π–π interfacial coupling boosts carrier transfer.

Sufficient active sites are needed for the reactants to be easily accessible, after the electrons have moved to the catalyst surface. The inherently high specific surface area and interconnected pore channels of MOFs and COFs further facilitate the efficient transport of CO_2 and H_2O (or other electron donors) to the active sites. Using these structural benefits, metal nanoparticles can be introduced into MOFs and COFs to improve catalytic activity. Han and coworkers developed Pt/Au@Pd@MOF-74 by encapsulating Au@Pd within MOF-74, with additional Pt nanoparticle deposition on its surface.[58] The CO_2 reduction efficiency and product selectivity were markedly enhanced in comparison to the usage of MOF-74 alone. Finally, the introduction of atomically dispersed metal sites (ADMSs) into MOFs and COFs enables strong interactions with CO_2 and suppresses undesirable side reactions.[59] For instance, Zhong *et al.* incorporated a single Ni active site into a COF (TpBpy) containing 2,2-bipyridine.[60] The COF facilitated CO_2 adsorption *via* its porous architecture, while the Ni active sites established a strong bond with CO_2, promoting its conversion into CO. As a result, it generated 4057 μmol g^{-1} of CO for 5 h with 96% selectivity. Examples in Sections 3.3 and 4.3 show how MOF- and COF-derived structures optimize catalytic sites for stable and efficient CO_2 photoreduction.

The efficiency of the CO_2 reduction reaction can be maximized by using various strategies to improve catalytic performance by combining the advantages of MOFs and COFs with the properties of other materials. The following section will discuss adjusting appropriate strategies to design MOFs and COFs and their effects on catalytic properties.

3. MOF-based photocatalysts

MOFs have received significant attention as photocatalysts in recent years. The superior photocatalytic performance of MOFs is attributed to their unique physical and chemical properties;[25,61–63] (i) MOFs offer numerous combinations of organic ligands and metal nodes. Consequently, energy bandgaps can be modified to improve photocatalytic activity; (ii) high porosity and large specific areas of MOFs provide an abundance of active sites. Moreover, the inherent pore structure promotes CO_2 adsorption; (iii) high CO_2 adsorption capacity in many MOFs can increase the CO_2 concentration around catalytic active sites and thereby enhance reaction efficiency. The selection and modification of organic ligands and metal nodes significantly influence the performance of the photocatalyst. Moreover, MOFs exhibiting limited photoactivity can be integrated with additional components (such as semiconductors, photosensitizers, single atoms, *etc.*) to create MOF-based composites or transformed into MOF derivatives to enhance the efficiency of photoreactions. Herein, photocatalytic MOFs are categorized into 3 sections and summarized (Table 1).

3.1. Pristine and functionalized MOFs

Research on MOF-based photocatalysts has been active since 2007, when Garcia *et al.* showed that MOF-5 exhibited the behaviour of a semiconductor, indicating its potential as a photocatalyst.[64] MOFs' remarkable tunability allows them to optimize their catalytic effectiveness while forming various structures based on their composition and synthesis circumstances. The morphology of MOFs significantly influences the photocatalytic performance by affecting light absorption, charge transfer efficiency, and the exposure of active sites. The charge transfer pathways and catalytic properties were optimized by controlling the crystal planes in NH_2-MIL-125(Ti).[68] The ratio of {001} to {111} planes of NH_2-MIL-125(Ti) can be regulated by adjusting the solvent composition ratio and the reaction conditions (Ti source, use of a modulator) during synthesis. The differences in crystal planes significantly influenced the properties of charge transfer and the catalytic active sites of the MOF. The calculated HOMO–LUMO values indicate that the {111} plane of NH_2-MIL-125(Ti) exhibits the smallest energy gap, resulting in enhanced photo response (Fig. 3a). In addition, the CO_2 adsorption capacity and the exposure concentration of Ti^{3+} increase, providing a strong reducing power. As a result, the {111} dominant sample showed a CO production rate nine times higher than the {001} dominant sample. Other than the crystal morphology and structure of MOFs, the layered structure can be used. Liang's group enhanced photocatalytic performance by designing a bilayer structure using a 2D MOF.[45] The bilayer MOF has a staggered layer structure, and Cl^- ions connect the layers and stabilize the structure. The bilayer MOF exhibits low CO_2 adsorption energy, allowing smooth charge transfer. The research findings indicate that the performance of CO_2 reduction can be significantly enhanced by implementing MOFs' intrinsic physical and chemical properties through structural optimization. Porphyrin-based MOFs are photosensitive organic compounds commonly used in MOF photocatalysis.[96–98] Porphyrins have significant light absorption properties over a wide wavelength range, and when combined with metal nodes, they can provide good electron transfer paths, maximizing catalytic efficiency.[96,98] Chen *et al.* proposed a strategy to enhance the catalytic performance of CO_2 reduction by optimizing charge transfer between porphyrin ligands and Zr-O clusters (PCN-233).[65] PCN-233 showed light absorption in a broad wavelength range (200–750 nm) due to its porphyrin ligands, and it possessed a narrow band gap of 1.68 eV. By absorbing light and transferring electrons to metal clusters, the ligand-to-metal charge transfer (LMCT) process suppresses electron–hole recombination and the ligands themselves serve as catalytic active sites (Fig. 3b). Therefore, both the ligand and the metal function as catalysts, demonstrating significant catalytic efficiency. The $HCOO^-$ production rate of PCN-233 is 65.2 μmol g^{-1} h^{-1}, showing superior performance compared to the existing Zr/Ti-MOF under identical conditions. LMCT describes an electronic transition in which an electron moves from a ligand-based orbital to a metal-based orbital within a coordination compound, often following light absorption.[99]

MOFs can be structurally optimized by combining diverse metal nodes and organic ligands, employing various synthetic techniques. However, the performance of MOFs can be further adjusted through post-synthetic modification (PSM) such as ligand substitution, metal substitution, and doping after synthesis.[100,101] Kong *et al.* employed porphyrin ligands to enhance MOFs' chemical stability and catalytic performance.[46] To address the low chemical stability of the BUT-109(Zr), the porphyrin ligand was incorporated into a MOF *via* ligand substitution ($NDIDB^{2-} \rightarrow DCPP^{2-}$). As the porphyrin concentration increased, the structurally stronger covalent bond was maintained, and the MOF structure remained stable over pH 1–10. The CO_2 uptake capacity improved with higher porphyrin content (Fig. 3c), as the porphyrin ligand provides a strong affinity for CO_2 molecules. The researchers performed experiments to enhance catalytic performance by varying the metal center to Ni, Co, Fe, and Cu, along with modifying the ligand of the MOF. Among these, the Co MOF showed the highest catalytic performance and selectivity (Fig. 3d). Additionally, in the recycling test, BUT-110–50%-Co showed no significant variation in CO production during five catalytic cycles

Table 1 Photocatalytic CO_2 reduction performance of MOF-based catalysts

	Photocatalyst	Light source	Efficiency (μmol g^{-1} h^{-1})	Selectivity	AQY[a] (at λ/nm)	TOF[b] (h^{-1})	Ref.
Pristine MOF	BUT-110–50%-Co	300 W Xe lamp (320–780 nm)	CO: 64	89%	N/A	N/A	46
	Ni-MOF(H_2O)	5 W white LED lamp (400–1000 nm)	CO: 9.61	95.24%	1.28% (420)	N/A	53
	PCN-223	300 W Xe lamp (420–800 nm)	$HCOO^-$: 65.2	N/A	N/A	N/A	65
	Bilayer nMOF 2	300 W Xe lamp	CO: 112.25	100%	N/A	N/A	45
	UiO-66-NH_2 (Cu-MOF)	300 W Xe lamp ($\lambda > 420$ nm)	CH_3COCH_3: 70.9	97.1%	N/A	N/A	66
	Co-OAC	300 W Xe lamp ($\lambda > 380$ nm)	CO: 2325.7	99.1%	N/A	14.4	67
	NH_2-MIL-125(Ti) (NM_{111})	300 Xe lamp (AM 1.5G)	CO: 8.25, CH_4: 1.01	N/A	N/A	N/A	68
	0.25MIL-101-F,F	300 W Xe lamp ($\lambda > 420$ nm)	CO: 688	N/A	N/A	N/A	69
	Ni-74-Am	300 W Xe lamp ($\lambda > 400$ nm)	CO: 1380	94%	N/A	N/A	70
MOF composite	CuTCPP $\subset$ UiO-66/TiO_2 (CTU/0.6TiO_2)	Xe lamp ($\lambda > 300$ nm)	CO: 31.32 CH_4: 0.148	N/A	N/A	N/A	71
	In-MOF@TP-TA	300 Xe lamp	CO: 25 CH_4: 11.67	N/A	N/A	N/A	72
	Co-MOF/Cu_2O (*x*CMC)	300 W Xe lamp ($\lambda > 420$ nm)	CO: 3.38	100%	N/A	N/A	73
	Cu-ZnTCPP/g-C_3N_4	300 W Xe lamp ($\lambda > 360$ nm)	CO: 92 CH_4: 11.3	N/A	N/A	N/A	74
	NM/*n*-WO_{3-x}	300 Xe lamp	CO: 12.57 H_2O_2: 8.41	N/A	0.17% (365)	N/A	75
	$Cs_3Bi_2Br_9$/Bi-MOF	300 Xe lamp	CO: 572.24 CH_4: 37.5	82.6%	N/A	N/A	76
	MOF-808-PBA-MV	300 W Xe lamp ($\lambda > 420$ nm)	CH_4: 460	99%	N/A	N/A	77
	Ru@Cu-HHTP	Xe lamp ($\lambda > 400$ nm)	CO: 130	92.9%	N/A	N/A	78
	Ir_1/A-aUiO membrane	300 W Xe lamp ($760 > \lambda > 420$ nm)	HCOOH: 3.38	99.4%	15.76% (420)	N/A	59
	Cu_2O@$Cu_3(BTC)_2$	500 W Xe lamp ($\lambda > 400$ nm)	[c]CH_4: 0.09125	N/A	N/A	N/A	79
	Zr-MBA-Ru/Re-MOF	300 W Xenon lamp (400–800 nm)	CO: 440	99%	0.11% (450)	N/A	80
	MOF-808-CuNi	300 W Xe lamp ($760 > \lambda > 420$ nm)	CH_4: 158.7	97.5%	2.31% (420)	N/A	81
	PQ-$CDs_{6.67}$@Cu-TCA	300 W Xe lamp ($\lambda > 420$ nm)	CH_4: 44.43	90.22%	3.35% (700)	N/A	82
	50-$Bi_4O_5Br_2$/Bi-MOF	300 W Xe lamp	CO: 23.78 CH_4: 2.39	N/A	N/A	N/A	83
	[DMC@cMOF]-PVK	300 W Xe lamp ($\lambda > 400$ nm)	CO: 133.36	N/A	N/A	N/A	84
MOF derivate	H-Co_3O_4/In_2O_3	300 W Xe lamp ($\lambda > 420$ nm)	CO: 4828	80%	0.59% (450)	N/A	85
	$Ni(OH)_2$-NC-2	100 W LED lamp	CO: 144000	96.1%	N/A	N/A	86
	Fe@C	300 W Xe lamp	CO: 26120	99.9%	N/A	N/A	87
	In_2S_3–$CdIn_2S_4$	300 W Xe lamp ($\lambda > 400$ nm)	CO: 825	N/A	N/A	N/A	88
	$ZnIn_2S_4$–In_2O_3	300 W Xe lamp ($\lambda > 400$ nm)	CO: 3075	N/A	N/A	N/A	89
	ZnO@Co_3O_4	300 W Xe lamp	CH_4: 0.99	N/A	N/A	N/A	90
	In_2O_3–C/$CdIn_2S_4$	300 W Xe lamp ($\lambda > 400$ nm)	CO: 2432	75.4%	0.93% (420)	N/A	91
	NPC-MoS_2@$Bi_4O_5Br_2$	250 W high-pressure mercury lamp (λ = 380 nm)	CO: 95.8 CH_4: 159.9	N/A	N/A	N/A	92
	In_2O_3@InP_{60}/Cu_2O−1	300 W Xe lamp	CH_4: 38.8	91.9%	N/A	N/A	93
	$In_{2-x}S_3$/$Cd_{1+x}In_{2-x}S_4$	300 W Xe lamp ($\lambda > 400$ nm)	CH_4: 132.5 CO: 392.1	N/A	N/A	N/A	94
	c-In_2O_3	300 W Xe lamp ($\lambda > 320$ nm)	CO: 29.19	94.47%	N/A	N/A	95

[a] Apparent quantum yield. [b] Turnover frequency. [c] The amount of photocatalyst wasn't specified.

(Fig. 3e) and maintained crystallinity and shape even after the catalytic reaction, demonstrating high stability. Xu *et al.* proposed a strategy to improve the PC CRR by utilizing a fluorinated MOF *via* ligand functionalization.[69] Pristine MIL-101(Fe) has high porosity and excellent CO_2 adsorption capacity, but its photocatalytic efficiency is limited due to poor electron transfer. To address this issue, fluorinated ligands (2-fluoroterephthalic acid and 2,5-difluoroterephthalic acid) were introduced to improve the electron transfer properties of MIL-101(Fe). The fluorinated MOF enhances hydrogen bonding with the photosensitizer ($[Ru(bpy)_3]^{2+}$), hence facilitating intermolecular electron transfer and improving the efficiency of the CO_2 reduction reaction. The fluorinated MOF showed a CO production rate of 688 μmol g^{-1} h^{-1}, which is about 3 times higher than that of pristine MIL-101(Fe). This demonstrates that fluorination can effectively enhance the photocatalytic performance of MOF-based catalysts. Researchers also confirmed that the same technique is applicable to additional Fe-based MOFs, such as MIL-53(Fe) and MIL-88(Fe), indicating the potential for improved catalytic performance by ligand engineering of MOFs. The catalytic activity of MOFs differs according to the electronic structure and coordination environment of

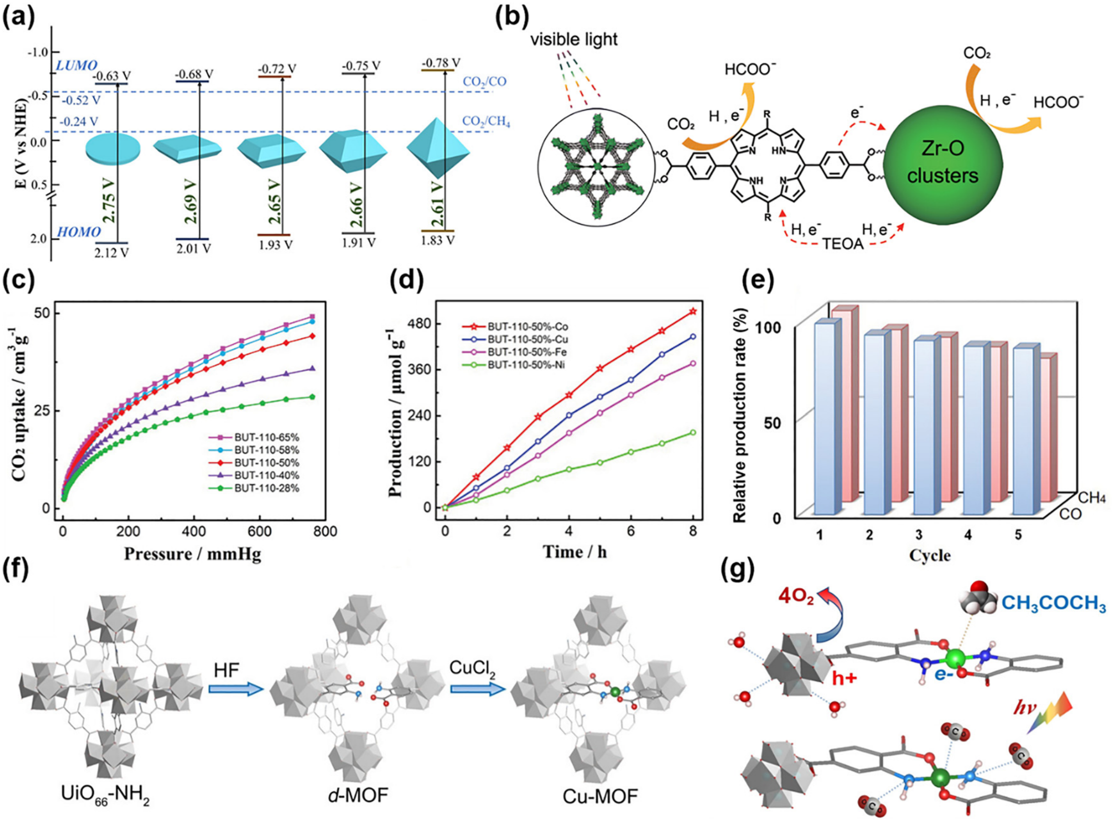

Fig. 3 Pristine and functionalized MOFs for photocatalytic CO_2 reduction reaction. (a) HOMO–LUMO gap of NH_2-MIL-125(Ti) with different exposed facets. Reproduced from ref. 68 with permission from American Chemical Society, copyright 2020. (b) Photocatalytic mechanism proposed for CO_2 reduction over PCN-223. Reproduced from ref. 65 with permission from Royal Society of Chemistry, copyright 2022. (c) CO_2 adsorption isotherms of BUT-110-X (X is the portion of the porphyrin ligand) samples. (d) BUT-110–50%-M with varied metal species under full-spectrum irradiation. (e) Relative production rate of CO and CH_4 obtained from CO_2 photoreduction over BUT-110–50%-Co catalyst in five cycles. Reproduced from ref. 46 with permission from Wiley-VCH, copyright 2021. (f) Synthetic procedure for the Cu-MOF. (g) The overall approach to reducing CO_2 into CH_2COCH_3 at CuN_2O_2 active sites under visible light irradiation. Reproduced from ref. 66 with permission from Wiley-VCH, copyright 2024.

the metal nodes. Sun *et al.* substituted Zn in the Zn-based MOF (CFA-1) with Co (Co-OAc, Co-Br, Co-CN), which has different coordination environments.[67] The oxidation states and spin states of Co varied among the three MOFs. According to X-ray photoelectron spectroscopy (XPS) and electron paramagnetic resonance (EPR), Co-OAc demonstrated the highest spin state. Co-OAc produced a CO with a high generation rate of 2325.7 μmol g^{-1} h^{-1} and a high selectivity of 99.1%, while the high spin state enhanced the charge separation efficiency and CO_2 adsorption. DFT calculations indicated that the high spin state inhibited electron–hole recombination and reduced the energy barrier for forming *COOH intermediates. In addition, superior electron mobility and high charge separation efficiency were attributed to low carrier density.

Zhang and co-workers used defect engineering to modify the active sites inside MOFs.[66] Cu^{2+} was incorporated into the defective UiO-66-NH_2 (d-MOF), forming NH_2-Cu-NH_2 ternary catalytic active sites (Fig. 3f). Upon light irradiation, Cu^{2+} accepts electrons and converts to Cu^+, which promotes electron transfer for CO porphyrin ligand reduction. The NH_2-Cu-NH_2 active sites subsequently adsorb CO_2, stabilizing CO and CH_3 intermediates and facilitating C–C bond formation (Fig. 3g). Finally, CO_2 is selectively converted to acetone (CH_3COCH_3) *via* a multi-electron reduction process, demonstrating a superior C_3 product formation rate of 70.9 μmol g^{-1} h^{-1} compared to UiO-66-NH_2 and d-MOF. Defect engineering could also be used to make defects in ligands. Dong *et al.* induced ligand defects in Ni-MOF-74 to increase the accessibility of metal active sites.[70] Ni-74-Am with an increased ligand defect density than Ni-MOF-74 was created by adjusting the synthesis temperature and solvent conditions. This improved the charge transfer properties and exposed more Ni active sites, which raised the catalytic activity. Ni-74-Am demonstrated 3 times higher CO_2 reduction performance than Ni-MOF-74, achieving a CO production rate of 1380 μmol g^{-1} h^{-1} and a CO selectivity of 94%. In addition, it was confirmed that the electron transfer rate was increased and charge recombination was suppressed in Ni-74-Am through photocurrent analysis. DFT calculation results showed that Ni-74-Am has lower CO_2 adsorption energy than the conventional Ni-MOF-74, and the formation of a COOH intermediate is more favorable, so that CO_2 reduction proceeds smoothly.

3.2. MOF composites

MOFs have a lot of benefits; however, their charge transportation and light absorption ability might be insufficient.

Producing MOF composites is a critical strategy to enhance MOFs' photocatalytic performance. MOF composites offer enhanced light absorption ability, electron mobility, charge separation efficiency, and reaction selectivity when paired with semiconductors, photosensitizers, COFs, QDs, *etc.*

Integrating MOFs with semiconductors has attracted interest as a method to enhance photocatalytic performance, utilizing the significant CO_2 adsorption abilities of MOFs with the superior charge transfer properties of semiconductors.[5,36] Cu_2O is a p-type semiconductor commonly used in photocatalysis. Cu_2O provides multiple advantages, including a narrow band gap and an extensive light absorption spectrum.[102,103] However, light and water vapor-induced corrosion reduces the catalyst's long-term stability.[104] Wu *et al.* employed a $Cu_3(BTC)_2$ MOF as a protective layer to create a core–shell structure protecting Cu_2O, hence enhancing the catalyst's durability.[79] Whereas Cu_2O without a MOF became amorphous due to photo-corrosion after the reaction, the composite preserved its crystalline. Additionally, the MOF coating improved CO_2 adsorption by 7 times, and the carboxyl ($-COO^-$) ligand established hydrogen bonds with the intermediate to stabilize it and improved charge separation. Cu_2O was also utilized by Dong and colleagues.[73] The synergy effect between MOFs and semiconductors can be maximized by forming a p–n heterojunction when Cu_2O and Co-MOF (which possess n-type semiconductor properties) are combined. Combining the Co-MOF and Cu_2O generates an internal electric field that promotes electron transfer and prevents charge recombination. Upon light exposure, the electrons produced in the conduction band (CB) of Cu_2O move to the CB of the Co-MOF and promote the PC CRR (Fig. 4a). In addition, the Co-oxo cluster acts as an electron storage, increasing the catalyst's electron density and CO_2 activation. Due to these structural attributes, the CO production rate of the Co-MOF/Cu_2O composite was 3.83 μmol g^{-1} h^{-1} and it had an almost 100% selectivity. WO_3 is a conventional n-type semiconductor that can modulate the Fermi level (E_f) by regulating oxygen vacancy (OV) concentration.[105] The introduction of a substantial quantity of oxygen vacancies (OVs) into WO_3 (WO_{3-x}) enhances light absorption, accelerates carrier separation, and has strong oxidizing power. However, the exclusive usage of WO_{3-x} has drawbacks, such as rapid charge recombination and low reducing power. Integrating WO_{3-x} with the NH_2-MIL-125(Ti) MOF to build an S-scheme heterojunction may resolve the limitations.[75] A built-in electric field (BEF) was generated between the two materials, which could be regulated by adjusting the concentration of OVs. The BEF was crucial for accelerating charge transfer and inhibiting charge recombination. As a result of the CRR, the NM/WO_{3-x} composite showed 8 times improved productivity of CO. A S-scheme heterojunction is an interface between two semiconductors engineered such that the system achieves both efficient charge separation and strong overall redox ability. This architecture combines features of type-II and Z-scheme heterojunctions: photogenerated charge carriers with weaker redox potential recombine at the interface, while high-energy electrons and holes accumulate on separate semiconductors, maximizing both charge separation and redox power.[56]

Immobilizing photosensitizers is another method that has been reported to enhance photocatalytic performance. For MOFs which require photosensitizers separately, the electron transfer efficiency is insufficient and needs a high concentration of photosensitizers. The close interaction of a photosensitizer with MOFs might expand the light absorption spectrum and optimize charge transfer, allowing more efficient utilization of visible light.[5,36] Huang *et al.* used electrostatic attraction to unite a cationic photosensitizer ($[Ru(phen)_3]^{2+}$) to the interior of an anionic MOF (Cu-HHTP) (Fig. 4b).[78] UV-vis study results showed increased absorption in the visible-light spectrum compared to the MOF alone. Furthermore, photoluminescence (PL) validated that charge transfer between the photosensitizer and MOF was very efficient. As a result, high catalytic activity was observed even at much lower photosensitizer concentrations. Karmakar's group utilized the pore structure of MOF-808 to optimize the electron transfer path by integrating not only the photosensitizer ($[Ru(bpy)_3]^{2+}$) but also the molecular catalyst ($[Re(bpy)(CO)_3Cl]$) by covalent bonds (Zr-MBA-Ru/Re-MOF).[80] MOF-808 has a nanometer (nm)-sized pore structure, allowing the close placement of catalytic active sites and the photosensitizer when both are immobilized within the pores. The composite prevents charge recombination and increases electron transport. In addition, MOF-808 could absorb light only in the UV range (200–320 nm), but the photosensitizer extended the light absorption range to the visible light range of 400–700 nm. As a result, the Zr-MBA-Ru/Re-MOF catalyst maintained high CO production selectivity (99%) and catalytic stability even without a sacrificial electron donor. After that, the same research team introduced 1-pyrenebutyric acid (PBA) and methyl viologen (MV) into the MOF pores to construct a charge transfer complex to optimize the charge transfer pathway and broaden the visible light absorption spectrum.[77] Consequently, MOF-808-PBA-MV showed significant light absorption in the 450–700 nm range and featured an electronic structure suitable to the CRR. Due to these modifications, MOF-808-PBA-MV exhibited improved efficiency compared to the original MOF in the selective reduction of CO_2 to CH_4, achieving 7.3 mmol g^{-1} of CH_4 production over 16 hours while sustaining a selectivity above 99%. Furthermore, photocurrent analysis and *in situ* diffuse reflectance infrared Fourier transform spectroscopy (DRIFTS) studies proved that electron transfer proceeded smoothly and the CO_2 reduction intermediate was efficiently stabilized.

Besides semiconductors and photosensitizers, complexation strategies, including diverse materials such as QDs, COFs, single atoms, *etc.*, are under active research. Ma *et al.* introduced a method to optimize CO_2 photoreduction efficiency through the covalent grafting of phenanthraquinone (PQ)-modified carbon quantum dots (CDs) onto a copper-based MOF (Cu-TCA MOF).[82] Despite the large porosity and CO_2 adsorption capacity of the standard Cu-TCA MOF, its photocatalytic activity was constrained by low conductivity and ineffective electron transport. To improve this, CDs were

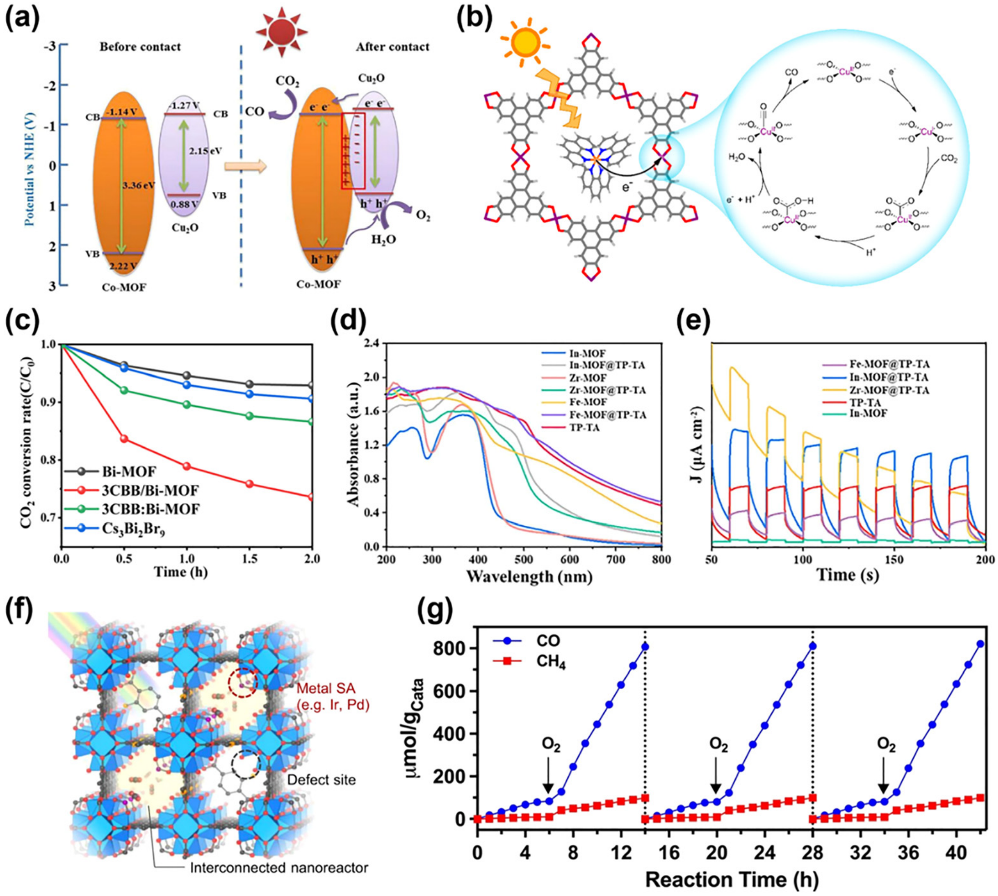

Fig. 4 MOF composites for photocatalytic CO_2 reduction reaction. (a) Schematic illustration of the electro-transfer process before and after contact with the Co-MOF/Cu_2O composite. Reproduced from ref. 73 with permission from Elsevier, copyright 2022. (b) Proposed reaction pathway of the photocatalyst Ru@Cu-HHTP. Reproduced from ref. 78 with permission from American Chemical Society, copyright 2021. (c) CO_2 conversion rate of $Cs_3Bi_2Br_9$, Bi-MOF, 3CBB/Bi-MOF, and 3CBB:Bi-MOF. Reproduced from ref. 76 with permission from American Chemical Society, copyright 2023. (d) UV-vis spectra and (e) transient photocurrent response to compare MOFs, COF, and MOF composites. Reproduced from ref. 72 with permission from Elsevier, copyright 2022. (f) Structure of Ir_1/A-$_a$UiO, defect-engineered MOF with single atom. Reproduced from ref. 59 with permission from Springer Nature, copyright 2021. (g) Cyclic experiment of PC CRR on pretreated Cu-ZnTCPP/g-C_3N_4, the gas atmosphere was switched between anaerobic and aerobic with in each cycle. Reproduced from ref. 74 with permission from Wiley-VCH, copyright 2023.

covalently grafted with Cu active sites to shorten the charge transfer distance, and additionally, dual-active sites and parallel charge transfer pathways were formed through PQ modification. As a result, PQ-CDs6.67@Cu-TCA showed a 2.47 times improvement in the electron consumption rate (393.98 μmol g^{-1} h^{-1}) compared to the Cu-TCA, and the CH_4 selectivity also increased up to 90.22%. Ding *et al.* proposed an approach for the *in situ* growth of $Cs_3Bi_2Br_9$ QDs on the surface of the Bi-based MOF (Bi-MOF) to form a strong interfacial interaction between the MOF and the QDs.[76] The bond formed between the MOF and QDs through the shared Bi atoms enhanced the electron transfer pathway and expanded the light absorption spectrum. Electrons were excited by light absorption from the $Cs_3Bi_2Br_9$, and they moved from the QDs to the MOF. Next, the CRR proceeded at the Bi active sites in the MOF. The $Cs_3Bi_2Br_9$/Bi-MOF showed enhanced efficiency in reducing CO_2 to CO compared to traditional MOFs (Fig. 4c). Yuan *et al.* integrated a conductive metal–organic framework (cMOF) with perovskite quantum dots (PVK QDs).[84] A dinuclear metal catalyst (DMC) was selectively placed within the pores of the MOF, and an ultrathin film structure was developed by immobilizing PVK QDs on the MOF surface to optimize the charge transfer path. The photoinduced electrons produced from PVK QDs were effectively transported to DMC active sites *via* the cMOF, suppressing charge recombination and resulting in enhanced selectivity and catalytic activity in the CRR. The optimized [DMC@cMOF]-PVK composite recorded a CO production rate of 133.36 μmol g^{-1} h^{-1}, which was more than 10 times higher than that of the conventional PVK or DMC-PVK catalysts.

Meanwhile, a COF has a unique π-conjugated structure and high charge mobility, and when combined with a MOF, it provides properties that can optimize the electron transfer path of the catalyst.[21,26,72] In particular, triazine-based COF (TP-TA) has excellent light absorption properties, and it promotes charge transfer. Wang and coworkers formed a type-II heterojunction by combining a TP-TA COF with three MOFs, respectively.[72] The UV-Vis indicated that the MOF–COF composite exhibited an enhanced light absorption range in the visible spectrum of 400–700 nm relative to the traditional MOF (Fig. 4d). Under light irradiation, electrons easily transferred from COF to MOF, and charge separation was promoted, which proved by transient photocurrent response (Fig. 4e). Then, electron–hole recombination was suppressed inside MOF and CRR was conducted at MOF's CB. As a result, the In-MOF@TP-TA composite showed the highest activity in the reaction of reducing CO_2 to CO (25.0 $\mu mol\ g^{-1}\ h^{-1}$) and CH_4 (11.67 $\mu mol\ g^{-1}\ h^{-1}$). Combining single atoms with MOFs is also an effective strategy. Individual atoms can act as separate active sites compared to traditional nanoparticle catalysts and have the advantage of sustaining high selectivity by modulating interactions with reaction intermediates. Hao *et al.* induced metal single atoms (Ir or Pd) in MOFs (Fig. 4f).[59] They generated defects in MOFs to allow single atom metals to act as catalytic active sites and fabricated a highly permeable MOF membrane. This structural change significantly improved the light absorption properties of MOFs. Unlike conventional MOFs that mainly react only in the ultraviolet region, the MOF membrane with single atoms could absorb visible light (over 600 nm). In addition, the single atom active sites facilitated electron transfer within the MOF and suppressed unnecessary electron–hole recombination. These modifications resulted in substantial enhancements in CO_2 reduction processes. Li *et al.* incorporated Cu/Ni dual-metal-site pairs (DMSPs) into MOF-808.[81] Conventional dual metal catalysts have a fixed active site structure, making it difficult to optimize the interaction with the reaction intermediate. To address this issue, self-adaptive DMSPs were developed by incorporating ethylenediaminetetraacetic acid (EDTA) into the Zr-oxo clusters inside the MOF to generate flexible Cu/Ni active sites. This structural change improved the light absorption performance of the MOF and facilitated the electron transfer at the catalytic active sites. Compared to Cu or Ni single catalysts, the MOF-composite promoted the conversion of CO_2 to CH_4 more effectively and suppressed the formation of by-products. The creation of a Z-scheme heterojunction by integrating $Bi_4O_5Br_2$ with a Bi-based MOF (Bi-MOF) also can enhance the CO_2 photoreduction efficiency.[83] $Bi_4O_5Br_2$ and Bi-MOF were designed to be self-assembled to simultaneously utilize the high reducing power of $Bi_4O_5Br_2$ and the excellent CO_2 adsorption ability of the Bi-MOF. The optimized 50-$Bi_4O_5Br_2$/Bi-MOF composite catalyst showed an increased CO production rate (23.78 $\mu mol\ g^{-1}\ h^{-1}$) compared to pure $Bi_4O_5Br_2$ and increased CH_4 production rate (5.39 $\mu mol\ g^{-1}\ h^{-1}$) compared to Bi-MOF, and also exhibited high catalytic stability and reusability. In addition, the Z-scheme charge transfer mechanism was demonstrated by ESR, UPS, and band structure analysis, and it was confirmed that $Bi_4O_5Br_2$ acts as an electron reservoir to suppress electron–hole recombination and promote electron transfer.

The CRR *via* photocatalysis has attracted attention as a fundamental technique for sustainable fuel production; however, in most catalytic systems, the presence of oxygen (O_2) is an obstacle to the CRR. Due to the higher reducibility of O_2 compared to CO_2, the oxygen reduction reaction (ORR) competes with the CRR on the catalyst surface, hence diminishing the overall reduction efficiency.[74,106,107] Previous studies have explored strategies to obstruct O_2 or to introduce an extra layer that selectively adsorbs CO_2 to address this issue. However, these approaches have the disadvantage of requiring separate energy consumption and complex processes.[74,106,107] Xie's group proposed a unique approach to activate the catalyst using O_2 rather than removing oxygen.[74] This photocatalyst, integrating the copper–porphyrin-based MOF (Cu-ZnTCPP) with g-C_3N_4, can selectively convert CO_2 to CO and CH_4, despite the presence of O_2. The CRR showed a reaction rate five times greater in a 20% O_2 environment compared to an O_2-free environment (Fig. 4g), and the selectivity for converting CO_2 to CO and CH_4 was enhanced. The appearance was mostly attributed to the structural modification of the Cu active site. X-ray absorption fine structure (XAFS) and *in situ* infrared (IR) studies indicated that Cu nodes were hydroxylated when O_2 was reduced on the catalyst surface, and these hydroxylated Cu nodes acted as active sites to enhance the CRR activity. Pd(II)-porphyrin-based polymer-coated hollow TiO_2 (Pd-HPP-TiO_2) also demonstrates a significant advancement in the aerobic PC CRR.[108] Unlike typical photocatalysts that suffer from the competing ORR, Pd-HPP-TiO_2 maintained high CO_2 selectivity and catalytic efficiency even under aerobic conditions. This performance was attributed to the porous Pd(II)-porphyrin polymer (HPP) layer, which selectively adsorbed CO_2 while suppressing O_2-induced side reactions, thereby enhancing charge separation and electron transfer. As a result, Pd-HPP-TiO_2 exhibits a 4.5-fold increase in CH_4 production compared to conventional TiO_2 under identical aerobic conditions. These studies suggest the possibility of designing a practical photocatalyst that can directly utilize CO_2 from air without further purification. Despite this promising performance under aerobic conditions, porphyrinic linkers are known to be susceptible to O_2-induced photooxidative degradation and, in some cases, demetallation upon prolonged irradiation.[109] Such degradation can compromise long-term catalytic activity and structural integrity. Therefore, future studies should verify the durability of such systems through extended operational testing and post-reaction characterization. Addressing these stability concerns is essential for designing practical photocatalysts capable of directly utilizing CO_2 from ambient air without additional purification.

3.3. MOF-derived materials

MOF derived catalysts exhibit excellent performance in a variety of catalytic reactions due to their high surface area, tunable nanostructure, and porous nature. In particular, in the PC CRR, catalysts utilizing MOFs as precursors can maximize performance through effects such as band gap adjusting, increase reaction active sites and charge transfer facilitation.[5,31,36] The design strategies of MOF-derived catalysts and recent studies are discussed in this section. Designing MOF-derived catalysts as composite structures is a way to maximize the synergistic effect by combining the advantages of individual components. An $In_{2-x}S_3/Cd_{1+x}In_{2-x}S_4$ heterojunction was developed by Zeng *et al.* to enhance the performance of wastewater treatment and CO_2 reduction simultaneously.[94] The OV of $In_{2-x}S_3$ promoted charge transfer, and by combining with $Cd_{1+x}In_{2-x}S_4$ to construct a Z-scheme photocatalytic system, the CO and CH_4 production increased by more than twice that of the conventional In_2O_3. The crystal structure of In_2O_3 also could be the key factor to optimize the CO_2 photoreduction performance. Wang *et al.* proposed a strategy to control the crystal structure of In_2O_3 and optimize the CO_2 photoreduction performance through the phase-selective synthesis of MOF-derived catalysts.[95] Rhombohedral (rh-In_2O_3), cubic (c-In_2O_3), and mixed (rh/c-In_2O_3) structures can be selectively synthesized by controlling the heat treatment temperature using MOF (MIL-68(In)-NH_2) as a precursor. DFT calculation showed that the high charge transfer efficiency and low activation energy barrier affects catalytic activity. Moreover, the presence of surface functional groups (amino groups) of MOFs acts as an important factor inducing the formation of a specific phase during the heat treatment process. As a result of evaluating the CO_2 reduction performance according to the phase, c-In_2O_3 showed the highest CO production rate of 29.19 μmol g^{-1} h^{-1} and selectivity of 94.47%.

Han and coworkers used a MOF-on-MOF structure grown ZIF-67 on InOF-1 as a precursor and converted it into a hollow heterometal oxide (H-Co_3O_4/In_2O_3) through acid treatment and low-temperature oxidation (Fig. 5a).[85] The H-Co_3O_4/In_2O_3 maximized catalytic performance through the advantages of each component. Co_3O_4 provided an active site for photocatalytic reactions, while In_2O_3 enhanced CO_2 adsorption and increased electron transport, thereby limiting charge recombination. These researches suggested that MOF-derived multicomponent composites can play an important role in improving catalytic performance. Also, the hollow structure offered more exposed active sites, promoting more efficient catalytic reaction. Compared to traditional single oxide catalysts, the H-Co_3O_4/In_2O_3 exhibited enhanced selectivity and greater efficacy in reducing CO_2 to CO. The advantage of this hollow structure was also confirmed in the study by Su *et al.*[86] ZIF-8 was used as a precursor to create hollow $Ni(OH)_2$ nanocages ($Ni(OH)_2$-NCs) through ion exchange and corrosion with $NiCl_2$. The nanocage structure promoted light absorption by encouraging multiple internal reflections and increased the catalytic efficiency by exposing more active sites (Fig. 5b). UV-vis analysis results showed that $Ni(OH)_2$-NC had an extended absorption spectrum to the visible light (400–700 nm), which was attributed to the multiple light reflection and scattering effects. Moreover, the presence of a large amount of oxygen vacancies in the catalyst promoted CO_2 adsorption and charge transfer, which suppressed electron–hole recombination. $Ni(OH)_2$-NC demonstrated higher catalytic activity than bulk $Ni(OH)_2$, with a high CO production of 1.44×10^5 μmol g^{-1} h^{-1} and a selectivity of 96.1%. This activity is among the highest reported for MOF-based systems (Table 1). However, it is important to note that many reported record values are not directly comparable. For instance, higher apparent quantum yield (AQY) and productivity are often achieved under high-intensity monochromatic irradiation or with excess sacrificial agents, which do not reflect practical solar operational environments. It was clearly shown in Su's work that the photocatalytic activity degrades after 3 h as the photosensitizer was deactivated. The choice and concentration of sacrificial reagents can artificially boost product yields, and some sacrificial agents can even serve as unintended carbon sources, leading to overestiation of genuine CO_2 reduction activity.[110,111]

Metal oxides derived from MOFs have the benefit of controllable nanostructures while maintaining high crystallinity. Zhao *et al.* synthesized an In_2O_3-C/$CdIn_2S_4$ (IOC/CIS) heterojunction by growing $CdIn_2S_4$ on In_2O_3-C, derived from a MOF (In-MIL-68) to optimized the CO_2 reduction activity.[91] In_2O_3 has high chemical stability, however it has a wide band gap (2.8 eV) that limits visible light absorption. To overcome this issue, $CdIn_2S_4$ was bonded to form a type-II heterojunction structure. As a result, charge recombination was suppressed, and the CRR was accelerated. In particular, carbon doping enhanced charge transfer and increased the CO_2 adsorption amount, recording a CO production amount of 2432 μmol g^{-1} h^{-1}. Sulfide-based catalysts have relatively narrow band gaps and excellent conductivity, and it is easy to form a heterojunction structure for

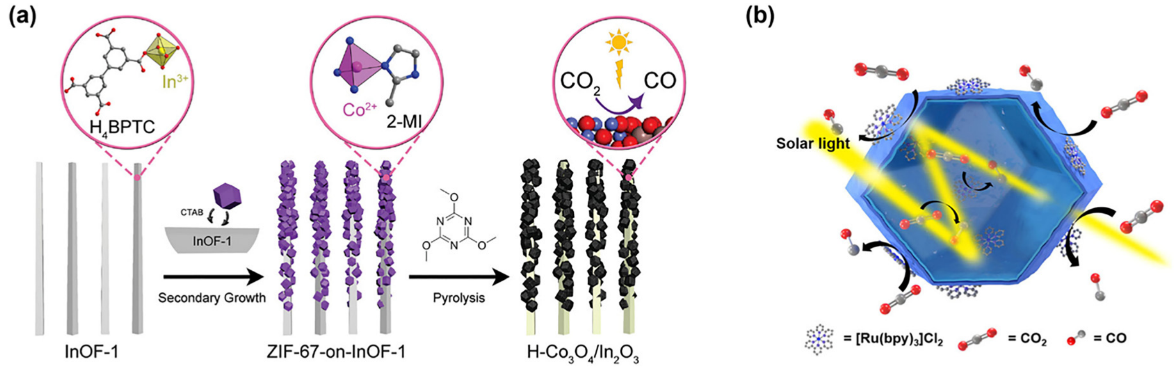

Fig. 5 MOF derivatives for photocatalytic CO_2 reduction reaction. (a) Stepwise fabrication of MOF-on-MOF-derived hollow bimetallic photocatalyst H-Co_3O_4/In_2O_3 for the PC CRR. Reproduced from ref. 85 with permission from Wiley-VCH, copyright 2023. (b) Structure-facilitated multiple light reflection and static charge-transfer processes of MOF-derived photocatalyst $Ni(OH)_2$-NC-2. Reproduced from ref. 86 with permission from American Chemical Society, copyright 2020.

improved charge separation. Sun and colleagues fabricated a p–n heterojunction structure (NPC-MoS_2@$Bi_4O_5Br_2$) by combining $Bi_4O_5Br_2$ and MoS_2 nanorods derived from the Mo-MOF to improve the CO_2 reduction performance.[92] NPC-MoS_2@$Bi_4O_5Br_2$ had a hierarchically bonded structure of 1D MoS_2 nanorods and 2D $Bi_4O_5Br_2$ nanoflakes, and MoS_2 acted as an electron transfer mediator to promote charge transfer. At the optimal composition containing 5% MoS_2, CO production of 95.8 μmol g^{-1} h^{-1} and CH_4 production of 159.9 μmol g^{-1} h^{-1} were recorded without additional photosensitizers or cocatalysts, showing a significant improvement in performance compared to the conventional $Bi_4O_5Br_2$. Phosphide-based catalysts have attracted attention in the CRR due to their high conductivity and excellent charge transfer ability. Xu's team developed In_2O_3@InP/Cu_2O dual Z-scheme photocatalysts to minimize electron–hole recombination.[93] While In_2O_3 has strong oxidizing ability, InP has a narrow band gap (1.35 eV) that increases the visible-light utilization. By depositing p-type Cu_2O onto the catalyst, the Z-scheme charge transfer mechanism was induced, which enhanced the conversion of CO_2 to CH_4 up to 91.9%.

4. COF-based photocatalysts

COFs were discovered approximately a decade after MOFs and have only recently been explored for photocatalytic applications.[18] Like MOFs, COFs offer advantages such as tunability, high porosity, large surface area, and high crystallinity. Moreover, when used as photocatalysts, COFs provide additional benefits compared to MOFs.[17] Specifically, the strong covalent bonds between monomers endow COFs with superior chemical and thermal stability relative to MOFs. Furthermore, the π-conjugated structure of COFs enhances charge carrier mobility in-plane and stacking directions, thereby improving electrical conductivity. Considering these numerous advantages, this chapter examines the research developments undertaken to advance COFs for CO_2 photoreduction. The production rate and selectivity of COF-based photocatalysts are summarized in Table 2.

4.1. Pristine and functionalized COFs

COFs with intrinsic light-absorbing capabilities can be directly utilized even in their pristine state. Among these, some COFs exhibit a metal-free composition, which results in lower density and cost-effectiveness. Baeg and co-workers were one of the pioneering research teams that explored COFs for CO_2 photoreduction.[131] The group synthesized a triazine-based, metal-free, two-dimensional COF *via* condensation polymerization between cyanuric chloride and perylene diimide. By drop-casting COF onto polyimide substrates, they fabricated a large-area flexible film photocatalyst demonstrating 3.4 times increase in HCOOH production compared to the monomers. The polymeric structure with a band gap of 2.05 eV and an ordered π-electron channel enabled effective PC CRR. However, due to the limited catalytic activity, converting CO_2 molecules necessitated the regeneration of nicotinamide adenine dinucleotide (NAD^+/NADH). In contrast, COFs capable of converting CO_2 and H_2O into CH_3OH without any sacrificial agent have also been reported.[47] Using triformylbenzene (TFB) and triazine, two distinct azine-based COFs were synthesized; both exhibited a higher CH_3OH production rate compared to the widely studied g-C_3N_4. Brunauer–Emmett–Teller (BET) and UV–Vis analysis revealed that the triazine-based COF possessed a larger specific surface area and a smaller band gap than its TFB-based counterpart, resulting in an enhanced visible-light sensitivity. Consequently, the triazine-based COF generated a higher photocurrent. This improvement is further attributed to the electron-deficient nature of triazine, which effectively stabilizes photogenerated electrons and enhances the photocatalytic activity. The extensive focus on triazine in this research area is largely due to its CO_2-philic properties. Similarly, to amine groups and imidazole groups, triazine had already been widely exploited for CO_2 capture. To achieve more effective band structure tuning and increased conductivity, Liu's group investigated heteroatom doping within the triazine-based framework.[122] By condensing hexachlorocyclo-triphosphazene (HCCP) with barbituric acid, they synthesized an N, O, P-containing covalent organic polymer (NOP-COP). Compared to the phosphorus-free counterpart (NO-COP), NOP-COP exhibited an extended lifetime of photoinduced charge carriers. Remarkably, CH_4 was produced as the sole carbonaceous product with a selectivity exceeding 90%. Moreover, the CB position of NOP-COP was more negative than that of NO-COP, thereby facilitating a more efficient PC CRR. It was also suggested that the high CO_2 affinity of the $-P{=}N$ groups promoted the adhesion and activation of CO_2 molecules. Also, intramolecular charge transport (ICT) in COFs can be enhanced by modifying the monomers. Lei *et al.* designed a donor–acceptor COF by linking an electron-rich moiety with an electron-deficient moiety.[41] This design enabled effective exciton dissociation and band gap modulation, resulting in a CO evolution rate of 102.7 μmol g^{-1} h^{-1} without any co-catalyst. DFT calculations further identified the nitrogen atoms within the triazine rings as the active sites. In contrast to the above findings, Wang's group proposed that the triazine ring functions as an electron reservoir while the imine bond serves as the catalytic center.[114] They argued that the powder-type samples used in previous studies contributed to discontinuous charge and mass transfer. As a solution, they fabricated a homogeneous COF membrane. To elucidate the roles of the structural units, the authors compared photocurrent density, PL intensity, and PL lifetime. These results demonstrated that increasing the number of triazine groups led to enhanced charge separation efficiency and prolonged lifetimes of photogenerated electrons while the recombination rate decreased (Fig. 6a). DFT calculations indicated that the LUMO is localized near the imine moiety, whereas the HOMO is concentrated on the triazine moiety. According to these findings, the imine moiety acts as an electron acceptor, while the triazine moiety functions as an electron donor and, at the same time, promotes the separation of photogenerated charge carriers. A similar research to Lei *et al.*'s work was conducted recently by Yu's group.[41] In this

Table 2 Photocatalytic CO_2 reduction performance of COF-based catalysts

	Photocatalyst	Light source	Efficiency (μmol g^{-1} h^{-1})	Selectivity	AQY[a] (at λ/nm)	TOF[b] (h^{-1})	Ref.
Pristine COF	Re-f-COF	Xe lamp ($\lambda > 420$ nm)	CO: 787.5	N/A	N/A	N/A	52
	Cu-Bpy-COF	60 W white LED lamp	CH_4: 17.5 in H_2O CO: 10.2 in DMF	CH_4: ∼100% CO: ∼100%	N/A	N/A	112
	Co-2,3-DHTA-COF	300 W Xe lamp ($\lambda > 420$ nm)	CO: 18 000	95.7%	0.47% (450)	111.8	15
	LaNi-Phen/COF-5	300 W xenon lamp (∼100 mW cm^{-2})	CO: 605.8	98.2%	N/A	N/A	113
	2N-COF	300 W xenon lamp (∼100 mW cm^{-2})	CO: 310	100%	0.36% (420)	N/A	114
	CoNi–COF-3	300 W Xe lamp ($\lambda > 420$ nm)	CO: 2567	92.2%	2.95% (450)	N/A	115
	MCOF-Ti_6Cu_3	300 Xe lamp (AM 1.5 cut-off filter)	HCOOH: 169.8	N/A	N/A	N/A	116
	Fe SAS/TrCOF	300 W Xe lamp ($\lambda > 420$ nm)	CO: 980.3	96.4%	3.17% (420)	N/A	16
	Mo-COF	300 W Xe lamp ($\lambda > 420$ nm)	CO: 6.19 CH_4: 1.08 C_2H_4: 3.57	CO: 57.10% CH_4: 9.96% C_2H_4: 32.92%	N/A	N/A	117
	COF-367-Co^{III}	300 W Xe lamp ($\lambda > 380$ nm)	HCOOH: 93	97.1%	N/A	N/A	118
	CT-COF	300 W Xe lamp ($\lambda > 420$ nm)	CO: 102.7	98%	0.104% (420)	N/A	41
	Re-Bpy-sp^2c-COF	300 W Xe lamp ($\lambda > 420$ nm)	CO: 1400	86%	0.5% (420)	N/A	21
	COF-367-Co NSs	300 W Xe lamp ($\lambda > 420$ nm)	CO: 10162	78%	N/A	N/A	119
	Ni-TpBpy	300 W Xe lamp ($\lambda \geq 420$ nm)	CO: 811.4	96%	0.3% (420)	N/A	60
	TTCOF-Zn	300 W Xe lamp ($800 > \lambda > 420$ nm)	CO: 2.06	100%	N/A	N/A	120
	DQTP COF-Co,	300 W Xe lamp ($\lambda \geq 420$ nm)	CO: 1020	59.4%	N/A	0.55	121
	DQTP COF-Zn	300 W Xe lamp ($\lambda \geq 420$ nm)	HCOOH: 152.5	90%	N/A	0.08	121
	NOP-COP	300 W Xe lamp ($\lambda \geq 420$ nm)	CH_4: 22.5	90.2%	0.32% (420)	N/A	122
	Re-CTF-py	300 W Xe lamp ($1100 > \lambda > 200$ nm)	CO: 353.05	N/A	N/A	N/A	123
	N_3-COF	500 W Xe lamp ($800 \geq \lambda \geq 420$ nm)	CH_3OH: 0.5708	N/A	N/A	N/A	47
	Re-COF	225 W Xe lamp ($\lambda > 420$ nm)	CO: ∼750	98%	N/A	N/A	124
	Tpy-COF-Co	300 W Xe lamp ($\lambda \geq 420$ nm)	CO: 426000	55.4%	2.14% (450)	524	125
	Cu_4COF-2	300 W Xe lamp ($\lambda > 420$ nm)	CO: 23.8	94.3	N/A	N/A	126
	EPCo-COF-AT	300 W Xe lamp	CO: 17700	97.8	0.49% (450)	54.89	127
	Co-THD-COF	300 W Xe lamp ($\lambda \geq 420$ nm)	CO: 9357	95.1	9.35% (420)	N/A	128
	H-COF-Ni	300 W Xe lamp ($\lambda \geq 420$ nm)	CO: 2847	96	0.9% (420)	N/A	129
	Ni-TAPT-COF	300 W Xe lamp ($\lambda \geq 420$ nm)	CO: 25500	98.8	1.62% (475)	31.6	130
	CTF	450 W Xe lamp ($\lambda > 420$ nm)	HCOOH: 881300	N/A	N/A	N/A	131
COF composite	GO-COF-366-Co	300 W Xe lamp ($\lambda > 320$ nm)	HCOOH: 1975 in acetonitrile, CO: 6525 in acetonitrile/H_2O	CO: 96.1% $HCOO^-$: 94.4%	N/A	N/A	132
	CdS/$BiVO_4$@T-COF	300 W Xe lamp ($720 \geq \lambda \geq 420$ nm)	CO: 183.8 H_2: 269.8	CO: 40.5 H_2: 59.5	1.1% (420)	N/A	133
	25% PRGO/TP-COF	300 W Xe lamp ($\lambda > 400$ nm)	CO: 9.762	N/A	N/A	N/A	134
	[Emim]BF_4@Zn-*S*-COF	300 W Xe lamp ($\lambda > 420$ nm)	CO: 267.95	97.6%	2.8% (420)	N/A	135
	MoS_2@COF-15	60 W white LED lamp	C_2H_6: 56.2	83.8%	0.03% (450)	N/A	136
	CdS@COF	Xe lamp ($\lambda > 420$ nm)	CO: 507.13	72%	0.21% (420)	N/A	137
	g-C_3N_4(NH)/COF	300 W Xe lamp ($\lambda > 400$ nm)	[c]CO: 11.25	90.40%	N/A	N/A	28
	Ru/TpPa-1	300 W Xe lamp ($800 \geq \lambda \geq 420$ nm)	HCOOH: 108.8	N/A	N/A	N/A	132
	COF-318-TiO_2	300 W Xe lamp ($380 \geq \lambda \geq 800$ nm)	CO: 69.67	N/A	N/A	N/A	138

[a] Apparent quantum yield. [b] Turnover frequency. [c] The amount of catalyst was not specified.

study, the electron donor (triphenylamine) and acceptor (trinuclear Cu units) were connected *via* π-conjugated vinylene linkage. Vinylene linkage is superior to imine linkage that are commonly used in COFs. The delocalization reduces the charge recombination rates and charge transfer resistances. The directional transfer of photogenerated electrons from triphenyl amine to redox centers was investigated by using *in situ* XPS. The well-defined pathway from electron-rich unit to π-conjugation and then to electron deficient unit in the crystalline structure was the key to the improved photocatalytic performance.

Strategies such as linker functionalization and non-metallic heteroatom doping of COFs have been used to increase light absorption ability and separation efficiency through electronic structure modulation. However, they have not been very effective in increasing their catalytic activity. The nitrogen-rich structure of COFs allows for anchoring the catalytically active site. The Re carbonyl complex has been used as a CO_2 reduction photocatalyst since 1983.[139] The *fac*-Re(bpy)$(CO)_3$L (bpy = 2,2′-bipyridine, L = monodentate ligand) undergoes reductive quenching of triplet metal-to-ligand charge transfer (3MLCT) excited state by triethanolamine (TEOA). Subsequently, CO_2 capture occurs with loss of L and electron donation by another one-electron reduced species.[140] Following the above process, Re or Ru complexes can produce CO with high selectivity and quantum yield. However, due to various disadvantages of

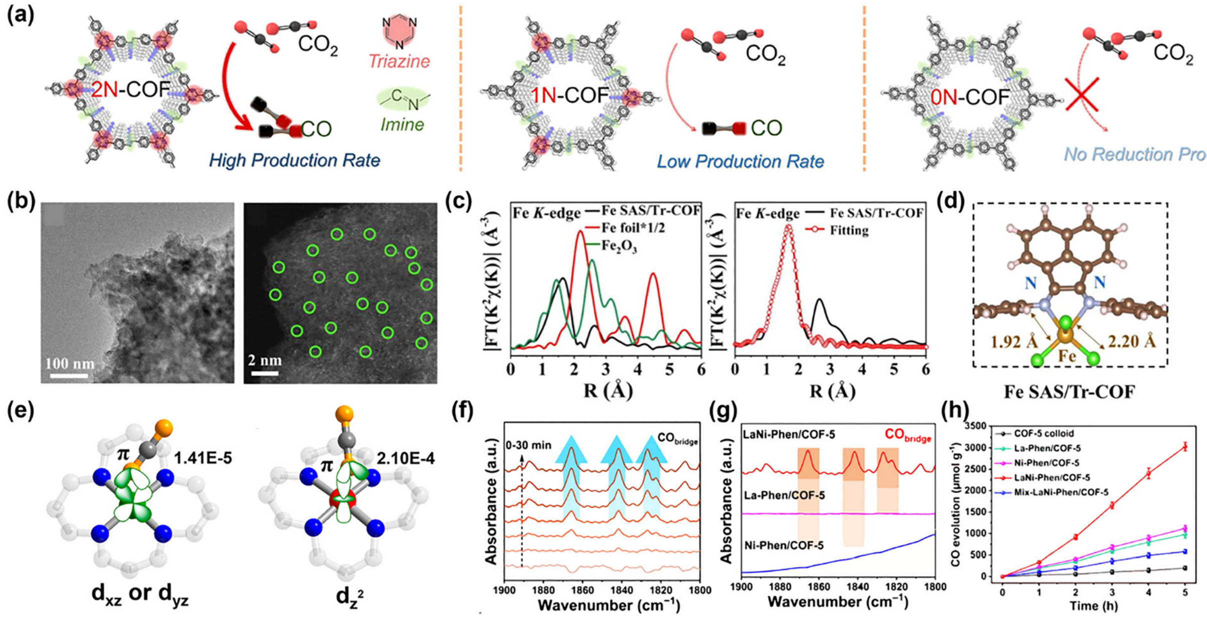

Fig. 6 Pristine and functionalized COFs for photocatalytic CO_2 reduction reaction. (a) Schematic illustration of 2N-COF, 1N-COF, and 0N-COF membranes. Reproduced from ref. 114 with permission from American Chemical Society, copyright 2023. (b) TEM and aberration-corrected HAADF–STEM image. (c) Fourier-transformed EXAFS spectra and the fitting curves in R space of Fe SAS/Tr-COFs. (d) Schematic model of Fe SAS/Tr-COFs. Reproduced from ref. 16 with permission from American Chemical Society, copyright 2022. (e) CO_2-adsorbed at Co sites with different spin states. Reproduced from reference with permission from American Chemical Society, copyright 2020. (f) *In situ* DRIFTS spectra of adsorbed CO on LaNi-Phen/COF-5. (g) DRIFTS spectra of adsorbed CO at 1800–1900 cm^{-1} over La-Phen/COF-5, Ni-Phen/COF-5, and LaNi-Phen/COF-5. (h) Time-dependent CO evolution curves under UV-vis light irradiation ($\lambda > 380$ nm). Reproduced from ref. 111 with permission from Springer Nature, copyright 2023.

homogeneous catalysts, such as non-recoverability, anchoring with COF as support has been investigated. Huang and coworkers synthesized an imine-linked Re-COF using 2,2-bipyridyl-5,5-dialdehyde (BPDA) and 4,4′,4″-(1,3,5-triazine-2,4,6-triyl) trianiline (TTA), followed by the reaction between the bipyridine ligand and $Re(CO)_5Cl$.[124] The Fourier transform infrared (FT-IR) spectroscopy spectrum and X-ray absorption spectroscopy (XAS) analysis confirmed the presence of $Re(bpy)(CO)_3Cl$, and no porosity or crystal structure changed. Due to the partial distribution of the excited ICT state in $Re(bpy)(CO)_3Cl$, photogenerated electrons transfer to the Re complex and the charge recombination is suppressed. The electrons with extended lifetime reduce CO_2 to CO_2 radical anion at the Re center. The addition of the catalytic active site enhanced the CO selectivity to 98%. However, the coordinated Re complexes suffered a significant mass loss in a solid–liquid system. After reaction in a mixed solution of anhydrous acetonitrile (MeCN) and TEOA, 57.2% of Re was leached out of the photocatalysts, and dissociated from the nitrogen coordination sites.[123] Xu *et al.* employed a solid–gas system instead to prevent Re leaching, and the system showed enhanced cyclic performance.[123] When measuring stability in a solid–gas system, the cumulative turnover number (TON) increased with each cycle. Another study utilizing $Re(bpy)(CO)_3Cl$ was conducted by Cooper's group.[21] Transient absorption spectroscopy showed that the presence of the Re center within the COF increased the lifetime of the charge separated state. A notable result of this study is that crystallinity and porosity have a significant impact on photoreduction performance. The use of 1,4-dioxane resulted in a highly crystalline COF, while in the mixture of 1,2-dichlorobenzene/1-butanol an amorphous analog was made. The amorphous polymer showed much lesser activity than crystalline COF even after being loaded with Re, due to the numerous structural defects that hinder charge transfer. In contrast, the crystalline structure and connected pore channels in the crystalline COF ensure the exposure of active sites for CO_2 adsorption and activation. The synthesis of COFs with π-conjugated structures plays a crucial role in their application as photocatalysts. Lu *et al.* compared the anchoring of other earth-abundant transition metals other than Re to COFs.[121] The strong bonding of Co, Ni, or Zn to two layers of appropriately spaced anthraquinone oxygen atoms results in immobilized active sites. The columnar orientation of the COFs makes an ordered π-electron pathway, with electrons efficiently transported to the metal moiety along the pathway, resulting in CO_2 reduction. The type of metal greatly affects the activity and selectivity. The Co active site produces mainly CO, while anchored Zn produces mainly HCOOH. According to the two-pathway mechanism proposed by the authors, Co(II), a good π-donor, weakens and breaks the C–O bond of the *COOH intermediate to form CO, while Zn(II), a poor π-donor, forms HCOOH. A total of seven metal elements were anchored to triazine-based COFs by Hou's group.[16] Among Fe, Co, Ni, Zn, Cu, Mn, and Ru, Fe had the highest CO generation rate of 980.3 μmol g^{-1} h^{-1}, 26 times higher than the pristine COF. Atomically dispersed Fe atoms could be identified by high-angle annular dark-field scanning transmission electron microscopy (HAADF-STEM) and Fourier-transformed extended X-ray absorption fine structure (EXAFS) (Fig. 6b and c). The bond lengths obtained from the optimized atomic structure model were also in good agreement with the EXAFS fitting results, confirming the existence of Fe–N bonding (Fig. 6d). By utilizing metalloporphyrin, the catalytic active site can be incorporated into the COF structure from the COF synthesis stage. Lan's group has enabled artificial photosynthesis through effective covalent coupling between electron-rich tetrathiafulvalene (TTF) and electron-deficient metalloporphyrin.[120] Through effective photoinduced electron transfer (PET), electrons reaching Zn generated CO, while in TTF, photogenerated holes triggered a water oxidation reaction to produce oxygen gas. Around the same time, Jiang's group developed a method for the bulk synthesis of metalloporphyrin and imine-based COF nanosheets.[119] By adding an excessive amount of 2,4,6-trimethylbenzaldehyde (TBA) in a solvothermal process hinders the π–π stacking, resulting in 2D COFs instead of bulk material. Compared to the conventional top-down approach of the exfoliation method, they have realized impressive high yield (> 55%) and large scale (> 100 mg) synthesis. Metalloporphyrins are frequently used due to the facile incorporation of single atomic metal sites with strong bonds and electrical interaction. Lin *et al.* also utilized Co, Ni, and Cu-containing perflourinated metallophtalocyanine and ellagic acid to demonstrate a photocatalyst with a high CO production rate.[127] Moreover, the post-synthetic treatment using an alkaline solution exposed the carboxylic anions and hydroxyl groups on the COF backbone and theoretical calculations suggest that the functional groups reduced the adsorption energy of CO_2 molecules. The COF sometimes acts as a host for the reactant and catalytic sites. In Zhong *et al.*'s work, electrons generated from the photosensitizer are transferred to a COF-supported single Ni site to cause CO_2 conversion.[60] Condensation of 1,3,5-triformylphloroglucinol and 5,5′-diamino-2,2′-bipyridine generate a 2,2′-bipyridine-based COF. Ni is incorporated by treating the COF in an acetonitrile solution containing $Ni(ClO_4)$. Interior cavities of the COF show high CO_2 capture ability due to the Lewis acid–base interaction between the CO_2 gas molecules and the coordinated Ni single atoms. Thereby the selectivity of CO production remains high at 76% even at low CO_2 partial pressure. The reduction of diluted CO_2 is important in a way that the concentrating process of CO_2 is expensive, and most of the point sources of greenhouse gases contain other gases, too. The effective adsorption and activation of CO_2 molecules are thus necessary. By chelating Ni atoms into the pre-designed imine–pyridine positions, the atomically dispersed active sites achieved a high CO selectivity of 98.8% even at 10% diluted CO_2 gas.[130] The use of 1,3,5-tris(4-aminophenyl) triazine (TAPT) led to a delocalization of the LUMO across the imine-pyridine moiety, making it an efficient electron acceptor. The incorporation of atomically dispersed metals suffered from the problem that the reaction product was limited to CO or syngas. The longer and heavier high-value hydrocarbons are produced, the better the cost-effectiveness of the system. In this regard, Kou and co-workers have done some interesting work.[117] They converted CO_2 to C_2H_4 with a high selectivity of about 33% at the MoN_2 active site bound to the dipyridyl site. At the Mo site, the CO_2 molecule is activated and undergoes a nonlinear conformational change. This lowers the energy barrier required to generate *CO. In addition, the strong adsorption between Mo and CO facilitated the subsequent process to C_2H_4. This is an impressive result because the more electrons required for conversion, the harder it is for the reaction to occur. The spin state of the metal atom can also change the reaction product selectivity. The cobalt embedded in COF-367 can have a spin ground state of 0 or 1/2 depending on the oxidation number of Co.[118] This changes the electron distribution/orientation of the Co 3d orbital. In the case of COF-367-Co^{II} (S = 1/2), $3d_{xz}$ or $3d_{yz}$ interacts weakly with the O 2p orbital of CO_2, while in COF-367-Co^{III} (S = 0), $3d_{z^2}$ strongly overlaps (Fig. 6e). The large difference in adsorption energy results in different catalytic activities and a much lower energy barrier for the transition states to undergo the HCOOH reaction pathway. Wang's group anchored the Co single atom to the hydroxyl group rather than the bipyridine site on the COF backbone.[15] The COF with the $Co–O_4$ site showed a benchmark performance of a CO production rate of 18 000 μmol g^{-1} h^{-1} with the help of Ru-based photosensitizer and sacrificial agent TEOA. The distinct coordination environment of Co(II) accelerated the electron transfer from the photosensitizer to the catalyst. Yue's group was inspired by carbon monoxide dehydrogenases and their coordination environment of metal active centers.[128] Thiophene and imine modules were used to anchor Co atoms onto the biomimetic coordination sites. The strong affinity of Co atoms to the CO_2 molecules ensured a higher local concentration of CO_2 at the catalytic sites. Also, the extended lifetime of the excited state and reduced charge recombination were evidenced by PL analysis. The researchers used actual seawater instead of deionized water to carry out PC CRR experiments. Due to the metal impurities and high concentration of chlorine ions, catalytic reactions in seawater often encounter significant degradation. However, the bioinspired photocatalyst maintained its structural and chemical state after an extended test in the natural seawater. Yang *et al.* also explored the effect of the microenvironment of metal active centers bonded to COF.[129] They found that in the experimented COFs, the affinity with CO_2 was much more influential to the photocatalytic activity when comparing the effect of the separation and transfer of charge carriers. The Ni–C bond length in the *N*-acylhydrazone linkage (3.074 Å) was shorter than the imine-linked counterpart (3.277 Å) according to DFT calculations, indicating the stronger affinity. Also, the stabilization of chelated Ni atoms in the five-membered ring prevented Ni leaching and ensured long-term photostability. Cu single site on COFs can also enhance light absorption, charge separation efficiency, and CO_2 adsorption and activation. More importantly, the reaction product, CH_4 or CO, depended on the solvent used, between H_2O and dimethylformamide (DMF).[112] The higher the ratio of H_2O to DMF, the lower the CH_4 selectivity, while the higher the CO selectivity. Similar results were observed in a cyclic test conducted over approximately 20 hours. The $^{13}CO_2$ labelling experiment confirmed that both CO and CH_4 originated from CO_2 gas. It was speculated that the selective products differed due to the difference in proton source and reaction mechanism. In DMF, the subsequent hydrogenation of *CO intermediate had a higher energy barrier (2.81 eV), producing CO without further reaction steps. However, in H_2O, the hydrogenation of triethylamine (TEA) required a much lower energy barrier (0.89 eV) for supplying hydrogen to the key reaction intermediate. Thus, *CO further reacted to form *CHO and CH_4. One of the most recent work on functionalizing COF is to improve the charge separation by modulating the direction of imine linkage in the COF backbone.[52] In a forward direction (f-COF), due to the polarization of the imine bond, the bipyridyl unit acts as an electron acceptor. On the other hand, in the reverse imine case (r-COF), the bipyridyl unit acts as an electron donor. In r-COF, $Re(bpy)(CO)_3Cl$ cannot receive electrons to cause a CRR, and charge recombination occurs rapidly. Therefore, the photocatalytic activity is negligible. The orientation of covalent bondings in COFs should be designed according to the same principle so that the separation of photogenerated charge carriers and ICT can occur efficiently. Instead of Cu single atoms, Xu *et al.* anchored a pre-synthesized tetranuclear Cu cluster on the organic skeleton.[126] When compared to the Cu MOFs with coordination driven assembly, the covalent linkage between metallic cluster and monomer displays high-stability characteristics. The long-term photoreduction test was performed for 12 hours without showing any decrease in the CO yield per hour, and the durability was retained for 6 cycles. The topology of the imine-based 2D cluster COFs was regulated, and the *qtz* topology showed higher CO yield and selectivity over dia topology, which was attributed to the more densely arranged structure. A benchmark CO production rate was achieved by Zhou's group.[125] A cobalt-anchored triazine framework reached 426 000 μmol g^{-1} h^{-1} for the first time, surpassing the results of preceding literatures. The high CO yield was attributed to the lowered energy barrier of the formation of key reaction intermediate, *COOH, on the $Co\text{-}N_4Cl_2$ site. The researchers also showed that the ratio of hydrogen and carbon monoxide in the syngas can be fundamentally regulated by changing the catalyst composition.

As high entropy alloys have received much attention in the field of catalysis, designing active sites using multiple metals can be expected to have a synergistic effect than using only one metal species.[141] Lan *et al.* arranged an oxidative cluster and a reductive cluster to achieve the interaction between two clusters efficiently.[116] By letting the CRR occur in the Cu cluster, and the water oxidation reaction occur in the Ti cluster, photoinduced charge separation and charge consumption can occur rapidly. The linkage due to the dynamic covalent bond between the two clusters was very effective for electron transfer. In some cases, two different metal species are both effective in the reductive reaction. Lan's group used Co and Ni to increase the catalytic activity and optimized the light absorption properties by adjusting the carbonyl groups of the building units comprising the COF.[115] In the CoNi-COF, the Ni sites enhanced CO_2 adsorption and promoted the formation of *COOH, while the Co sites were responsible for electron trapping and electron transfer to CO_2. The CO desorption energy was also reduced compared to a single metal, which mitigated the active site screening due to poisoning. The delocalization of the cross-linked framework and the push–pull effect facilitated charge transfer from the photosensitizer. Carbonyl groups enhanced the absorption properties of the COFs in the visible region, and the fully tautomerized COFs with a β-ketoenamine structure facilitated photogenerated charge transfer. *In situ* analysis monitors surface adsorbates and is necessary to obtain insights into reaction mechanism.[142] Zhou and co-workers used *in situ* DRIFTS analysis to reveal the presence of efficient CO adsorption sites only on the dual-atom catalyst (Fig. 6f).[113] *In situ* XAFS analysis revealed that La atoms are optically active centers and act as sites for CO_2 activation, with a reduction reaction occurring on Ni (Fig. 6g). Direct observation of the adsorbed/activated CO_2 and key reaction intermediates on the LaNi COF surface was also made possible (Fig. 6h).

4.2. COF composites

The modification of COFs is mainly done by adding catalytic active centers or modulating the structural units to change their electronic properties. By creating a composite of COFs and other materials, the charge separation efficiency in the heterojunction can be dramatically increased, and the bandgap difference allows a broader spectrum of light to be utilized. The most common inorganic semiconductor used with COFs is metal oxide. Metal oxide has several disadvantages compared to COFs when used alone, but they can work in synergy when used together. In a study by Zhang *et al.*, 3 different oxides were combined with COF-316/318 to construct a Z-scheme for artificial photosynthesis.[138] TiO_2, Bi_2WO_6, and Fe_2O_3 are all photocatalysts with good performance in water photooxidation and form a Z-scheme system with COF-318 due to the appropriate bandgap position. Therefore, the CO production rate is much higher than pure COF-318 or TiO_2. Notably, when the semiconductor was covalently coupled with COF *via* hydroxyl groups, the electron transfer was facilitated and the performance was superior to the simple physical mixture of these two materials. Many different COFs utilize imine linkages, but the strong polarization of the imine leads to poor delocalization of the π-electron. In a recent study by Wang's group, a semiconductor channel was demonstrated to be a possible solution to this challenge.[137] When CdS and COF were formed into a core–shell structure, photogenerated electrons from Zn–porphyrin were transported through the CdS to the CO_2 reduction site. The ICT *via* this new and efficient route resulted in a much more active PC CRR. The authors conducted control experiments in which the Zn–porphyrin, CdS, and Co-bipyridyl units were each removed to confirm the role of individual units. By comparing the bandgap values through UV-vis diffuse reflectance spectra, they found that the bandgap of CdS and COF changed after the heterostructure was created, indicating the existence of interfacial electronic interactions between the two materials. When MoS_2 forms a heterojunction with an anthraquinone-based COF, the interfacial e-field facilitates charge separation and transfer (Fig. 7a).[136] The hybrid composite, which used amino-modified MoS_2 to enhance the electronic interaction, produced hydrocarbon and ethane under visible light irradiation. When CO_2 adsorption–desorption measurement was performed, COF showed a high adsorption capacity of 62.7 $cm^3\ g^{-1}$, while MoS_2 showed negligible adsorption capacity due to its low porosity. MoS_2@COF showed similar adsorption behavior to COFs but 31.2 times more ethane production performance. *In situ* DRIFTS analysis of MoS_2@COF confirmed the existence of *COCO intermediate, and a high occurrence of C–C coupling was observed. The photocatalytic syngas production can be maximized when $BiVO_4$ (BVO) is inserted in addition to CdS and COF.[133] According to Fan *et al.*, radiative charge recombination is suppressed in the composite and charge transfer resistance is also reduced.[133] Based on the band alignment of the components, the CdS/COF composite has a single S-scheme system, and the CdS/COF/BVO composite has a dual S-scheme system. In the single S-scheme, CdS and COF have a weak internal electric field because the E_f difference is not large, so photoinduced electron and hole recombination occurs easily. On the other hand, in the dual S-scheme, severe band bending occurs at the heterojunction at CdS/BVO interface and COF/BVO interface, and strong internal electric fields are generated. Under illumination, the electrons of BVO and holes of CdS and COF at the interface are cancelled out, leaving only charge carriers for photoredox catalysis. CdS, BVO, and COF each play a different catalytic role. CO_2 reduction to CO occurs in COF, O_2 evolution in BVO, and H_2 production in CdS. The photocatalyst was synthesized with the help of a silica template for close interaction of the components, and the distribution of the elements was confirmed by scanning transmission electron microscopy energy-dispersive X-ray spectroscopy (STEM-EDS) mapping (Fig. 7b and c).

In addition to inorganic semiconductors, organic semiconductors such as graphitic carbon nitride are also useful for forming a favorable interface with COFs. Wang *et al.* utilized defective g-C_3N_4 to form van der Waals heterojunction with a triazine-based COF (Fig. 7d).[28] Nitrogen vacancy of the g-C_3N_4 increases the E_f gap between the two materials, which promotes the recombination of invalid photogenerated charge carriers. Meaningful electrons cause CO_2 conversion in g-C_3N_4. In the temperature-programmed desorption of CO_2 (CO_2-TPD) analysis, g-C_3N_4/COF exhibited a stronger CO_2 adsorption capacity than g-C_3N_4. Furthermore, while pristine g-C_3N_4 showed a sharp decrease in CO_2 conversion rate to below 30% during 7 h of irradiation, g-C_3N_4/COF showed a relatively more stable performance because of accelerated separation and transfer of photoinduced charge carriers. Similarly, photo-reduced graphene oxide (PRGO) and triazine-based COFs have a strong interaction to form a composite photocatalyst.[134] According to a study by Liu *et al.* PRGO and COF are combined through electrostatic self-assembly and have similar carbon skeletons, which leads to π–π stacking.[134] After heterojunction formation, electrons are transferred from the CB of PRGO to the valence

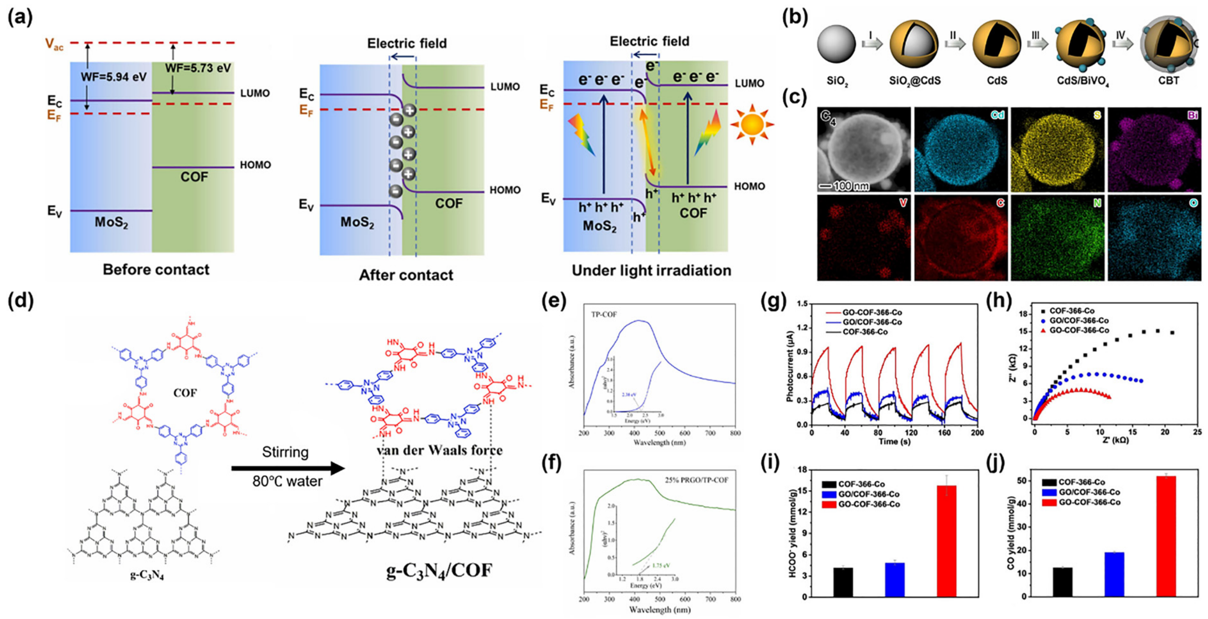

Fig. 7 COF composites for photocatalytic CO_2 reduction reaction. (a) Schematic illustrating the charge transfer process and the relative band positions of COF and MoS_2. Reproduced from ref. 136 with permission from Elsevier, copyright 2023. (b) Schematic illustration of the synthetic procedure and (c) STEM images and EDS-mapping profiles of CBT. Reproduced from ref. 133 with permission from Elsevier, copyright 2024. (d) Schematic illustration of g-C_3N_4/COF vdW heterojunction. Reproduced from ref. 28 with permission from Elsevier, copyright 2022. (e) DRUV–vis spectra of TP-COF and (f) 25% PRGO/TP-COF. Reproduced from ref. 134 with permission from Elsevier, copyright 2024. (g) Photocurrent tests and (h) EIS plots of GO-COF-366-Co, COF-366-Co, and GO/COF-366-C. (i) $HCOO^-$ yields and (j) CO yields after 8 h of reaction in CH_3CN. Reproduced from ref. 143 with permission from Wiley-VCH, copyright 2023.

band (VB) of COF, resulting in a BEF and band bending, which maximizes the separation efficiency of photogenerated charges. The light absorption was greater than the pristine COF (Fig. 7e and f). In the FT-IR spectrum, the peak caused by the vibration of tri-*s*-triazine is red-shifted, suggesting that the two materials form a composite and have a strong coupling interaction. For more intense cross-linking, covalent anchoring of COF on graphene oxide (GO) has also been studied. According to Gong *et al.*'s research, the formation of covalent bonds between COF-366-Co and GO shortens the charge transfer distance and reduces charge recombination, thereby increasing the catalytic activity (Fig. 7g–j).[143] FT-IR analysis confirmed the bond formed between the amine group of COF-366-Co and the functional group on the GO surface, and the binding energy shift in the XPS Co 2p spectrum demonstrated the strong interaction and charge transfer from COF to GO. They further identified a tendency for the reactant selectivity to change depending on the solvent. In CH_3CN, HCOOH was the major product with 94.4% selectivity, whereas in a solution mixed with H_2O, CO was generated with 96.1% selectivity.

The co-existence of COFs and metal nanoparticles can also be used to improve visible light harvesting and photocatalytic reduction of CO_2. Since Ru, a noble metal, is a good electron trap, it can accept electrons from the LUMO of the COF to improve charge separation.[132] However, excessive nanoparticle content may block the COF pores or interfere with light absorption. According to the photocurrent measurement, the best response was obtained when the weight percentage of Ru was 3%. Uniquely, some studies have utilized the abundant pores of COFs to create an interface with ionic liquids. Considering the commercialization and economic viability of CO_2 reduction, a high selectivity and conversion rate in dilute CO_2 mixed gas rather than pure CO_2 is required, and Yang's group realized an enriched CO_2 atmosphere through ionic liquid.[135] Ionic liquids have been previously used to load porous MOFs to increase their CO_2 absorption ability. In this study, CO_2 capture and photocatalytic conversion were integrated to create an overall more efficient system. Introducing 1-ethyl-3-methylimidazole tetrafluoroborate ([Emim]BF_4) into the Zn-*S*-COF allows the captured CO_2 to be supplied to the Zn active site. Calculations suggested that $Emim^+$ plays a role in supplying proton-electron pairs, which further promotes hydrogenation.

5. Conclusions and outlook

This review summarizes the latest research on MOFs and COFs used in the PC CRR. Compared to conventional photocatalysts such as metal oxides, MOFs and COFs have received much attention due to their advantages, such as high CO_2 adsorption capacity and recombination suppression resulting from their intrinsic porosity and high crystallinity. Among these advantages, design flexibility has played a major role in improving the properties and performance of MOFs and COFs. Various strategies such as linker functionalization, immobilizing photosensitizers, and metal node modification have been effective in regulating the electronic structure, including bandgap and increasing light utilization efficiency. Additionally, the formation of heterojunctions with organic or inorganic semiconductors has promoted favorable band alignment and interfacial electric fields to increase the lifetime of photoexcited charge carriers and facilitate their transfer to the redox centers. Embedding atomic metal sites and strengthening interactions between catalytic units have improved CO_2 adsorption and activation, stabilizing key intermediates.

Although many advances have been made in the light harvesting, charge transfer and catalytic activity of MOF and COF-based photocatalysts, several challenges remain. First, the products generated by the PC CRR are mostly CO or HCOOH. Recent studies have reported the production of C_{2+} hydrocarbons, such as ethane and ethylene. However, their production rates remain approximately three orders of magnitude lower than the established benchmark for CO production, indicating that further efforts are required to achieve economically and energetically viable multi-carbon products. For example, bimetallic active sites have been studied up to now, but the development of high-entropy active sites could be a breakthrough, where we can expect unprecedented synergistic effects between multiple elements. Secondly, an in-depth understanding of the reaction pathway is required. For hydrocarbon generation, it is necessary to design the microenvironment of the active site based on the understanding of the reaction mechanism rather than developing a photocatalyst by the trial-and-error method. In addition to *in situ* FT-IR, advanced analysis and prediction techniques such as *in situ* XAS, *in situ* TEM, DFT calculations and machine learning should be converged to create active sites capable of C–C coupling and multielectron processes. Also, many MOFs and COFs demonstrate promising performance under simulated light; however, their efficiency under full-spectrum sunlight often remains suboptimal. Bandgap engineering *via* π-conjugated linkers, donor–acceptor frameworks, and broadband light-harvesting units extends light absorption into the visible and near-infrared regions. Hierarchical pore architectures and photonic crystal-inspired morphologies enhance light trapping and scattering, thereby improving solar-to-chemical conversion efficiency under natural sunlight. Finally, only water should be used as an electron donor for the construction of an environmental-friendly and practical PC CRR system. Although organic sacrificial agents such as TEOA are often used to improve PC CRR performance, it is advisable to avoid using them due to toxicity and byproduct formation issues. Therefore, it is necessary to improve the structural stability in water and develop a photocatalyst with strong water oxidation ability. Structural reinforcement through robust metal–oxygen clusters (*e.g.*, Zr_6 and Ti_8) and covalent cross-linking of organic linkers can enhance framework stability and resilience. Surface hydrophobic functionalization or core–shell encapsulation can effectively mitigate environmental hydrolysis and photocorrosion, while integrating conductive and chemically stable supports helps maintain efficient electron transport pathways during prolonged operation.

Conflicts of interest

There are no conflicts to declare.

Data availability

No primary research results, software or code have been included and no new data were generated or analysed as part of this review.

Acknowledgements

This work was supported by the Nano & Material Technology Development Program through the National Research Foundation of Korea (NRF) funded by Ministry of Science and ICT(RS-2024-00405016) and the National Research Foundation of Korea (NRF) funded by the Ministry of Science and ICT (MSIT), South Korea (GTL25021-230). The Inter-University Semiconductor Research Center, Institute of Engineering Research, and SOFT Foundry at Seoul National University provided research facilities for this work.

Notes and references

1 P. N. Pearson and M. R. Palmer, *Nature*, 2000, **406**, 695–699.
2 S. Fang, M. Rahaman, J. Bharti, E. Reisner, M. Robert, G. A. Ozin and Y. H. Hu, *Nat. Rev. Methods Primers*, 2023, **3**, 61.
3 Y. Wang, E. Chen and J. Tang, *ACS Catal.*, 2022, **12**(12), 7300–7316.
4 Y. Zhang, D. Yao, B. Xia, M. Jaroniec, J. Ran and S. Z. Qiao, *ACS Energy Lett.*, 2022, **7**(5), 1611–1617.
5 R. Li, W. Zhang and K. Zhou, *Adv. Mater.*, 2018, **30**(35), 1705512.
6 Y. X. Pan, Z. Q. Sun, H. P. Cong, Y. L. Men, S. Xin, J. Song and S. H. Yu, *Nano Res.*, 2016, **9**, 1689–1700.
7 M. Reli, M. Kobielusz, L. Matějová, S. Daniš, W. Macyk, L. Obalová, P. Kuśtrowski, A. Rokicińska and K. Kočí, *Appl. Surf. Sci.*, 2017, **391**, 282–287.
8 Z. Xiong, Z. Lei, Z. Xu, X. Chen, B. Gong, Y. Zhao, H. Zhao, J. Zhang and C. Zheng, *J. CO$_2$* Util., 2017, **18**, 53–61.
9 Y. Yang, F. Zhan, H. Li, W. Liu and S. Yu, *J. Solid State Electrochem.*, 2017, **21**, 2231–2240.
10 Y. Ha, J. Kwon, H. An and D. Jung, *J. Sens. Sci. Technol.*, 2022, **31**, 343–347.
11 K. Ganesh Kumar, P. Balaji Bhargav, N. Ahmed and C. Balaji, *Trans. Electr. Electron. Mater.*, 2021, **22**, 717–724.
12 N. R. Khalid, S. Ilyas, F. Ali, T. Iqbal, M. Rafique, M. Imran and M. A. Assiri, *Electron. Mater. Lett.*, 2024, **20**, 85–94.
13 T. Hisatomi, J. Kubota and K. Domen, *Chem. Soc. Rev.*, 2014, **43**, 7520.
14 N. Shehzad, M. Tahir, K. Johari, T. Murugesan and M. Hussain, *J. CO$_2$* Util., 2018, **26**, 98–122.
15 Q. Zhang, S. Gao, Y. Guo, H. Wang, J. Wei, X. Su, H. Zhang, Z. Liu and J. Wang, *Nat. Commun.*, 2023, **14**, 1147.
16 L. Ran, Z. Li, B. Ran, J. Cao, Y. Zhao, T. Shao, Y. Song, M. K. H. Leung, L. Sun and J. Hou, *J. Am. Chem. Soc.*, 2022, **144**, 17097–17109.
17 T. Luo, L. Gilmanova and S. Kaskel, *Coord. Chem. Rev.*, 2023, **490**, 215210.
18 Z. He, J. Goulas, E. Parker, Y. Sun, X. Dong Zhou and L. Fei, *Catal. Today*, 2023, **409**, 103–118.
19 K. Endo, S. Canossa, F. Heck, D. M. Proserpio, M. S. Istek, F. Stemmler, J. van Slageren, S. Hartmann, A. Hartschuh and B. V. Lotsch, *Nat. Synth.*, 2025, **4**, 603–613.
20 A. Rodríguez-Camargo, M. W. Terban, M. Paetsch, E. A. Rico, D. Graf, R. Hirpara, V. Duppel, I. Moudrakovski, M. Etter, N. Guijarro, C. Ochsenfeld, R. E. Dinnebier, L. Yao and B. V. Lotsch, *Nat. Synth.*, 2025, **4**, 710–719.
21 Z. Fu, X. Wang, A. M. Gardner, X. Wang, S. Y. Chong, G. Neri, A. J. Cowan, L. Liu, X. Li, A. Vogel, R. Clowes, M. Bilton, L. Chen, R. S. Sprick and A. I. Cooper, *Chem. Sci.*, 2020, **11**, 543–550.
22 C. Zhang, Z. Lin, L. Jiao and H.-L. Jiang, *Angew. Chem., Int. Ed.*, 2024, **63**, e202414506.
23 Y. Li, H. Xu, S. Ouyang and J. Ye, *Phys. Chem. Chem. Phys.*, 2016, **18**, 7563.
24 S. A. Younis, E. E. Kwon, M. Qasim, K. H. Kim, T. Kim, D. Kukkar, X. Dou and I. Ali, *Prog. Energy Combust. Sci.*, 2020, **81**, 100870.
25 H. Zhang, J. Li, Q. Tan, L. Lu, Z. Wang and G. Wu, *Chem. – Eur. J.*, 2018, **24**, 18137–18157.
26 S. Liu, M. Wang, Y. He, Q. Cheng, T. Qian and C. Yan, *Coord. Chem. Rev.*, 2023, **475**, 214882.
27 S. Wang, J. Lin and X. Wang, *Phys. Chem. Chem. Phys.*, 2014, **16**, 14656–14660.
28 J. Wang, Y. Yu, J. Cui, X. Li, Y. Zhang, C. Wang, X. Yu and J. Ye, *Appl. Catal., B*, 2022, **301**, 120814.
29 K. K. Khaing, D. Yin, Y. Ouyang, S. Xiao, B. Liu, L. Deng, L. Li, X. Guo, J. Wang, J. Liu and Y. Zhang, *Inorg. Chem.*, 2020, **59**, 6942–6952.
30 S. Yan, S. Ouyang, H. Xu, M. Zhao, X. Zhang and J. Ye, *J. Mater. Chem. A*, 2016, **4**, 15126–15133.
31 J. Chen, R. Abazari, K. A. Adegoke, N. W. Maxakato, O. S. Bello, M. Tahir, S. Tasleem, S. Sanati, A. M. Kirillov and Y. Zhou, *Coord. Chem. Rev.*, 2022, **469**, 214664.
32 L. Hu, H. Yang, S. Wang, J. Gao, H. Hou and W. Yang, *J. Mater. Chem. C*, 2021, **9**, 5343–5348.
33 S. Li, J. Tan, Z. Jiang, J. Wang and Z. Li, *Chem. Eng. J.*, 2020, **384**, 123354.
34 M. Lan, R. M. Guo, Y. Dou, J. Zhou, A. Zhou and J. R. Li, *Nano Energy*, 2017, **33**, 238–246.
35 Q. Su, Q. Guo, H. Wang, M. Liu and C. Zuo, *Carbon Resour. Convers.*, 2024, **7**(1), 100211.
36 D. Li, M. Kassymova, X. Cai, S. Q. Zang and H. L. Jiang, *Coord. Chem. Rev.*, 2020, **412**, 213262.
37 Y. He, L. Yin, N. Yuan and G. Zhang, *Chem. Eng. J.*, 2024, **481**, 148754.
38 G. H. Han, J. Bang, G. Park, S. Choe, Y. J. Jang, H. W. Jang, S. Y. Kim and S. H. Ahn, *Small*, 2023, **19**, 2205765.
39 L. Zhang, J. Ran, S. Z. Qiao and M. Jaroniec, *Chem. Soc. Rev.*, 2019, **48**, 5184.
40 W. Huang, W. Luo and Y. Li, *Mater. Today*, 2020, **40**, 160–172.
41 K. Lei, D. Wang, L. Ye, M. Kou, Y. Deng, Z. Ma, L. Wang and Y. Kong, *ChemSusChem*, 2020, **13**, 1725–1729.
42 D. Wang, R. Huang, W. Liu, D. Sun and Z. Li, *ACS Catal.*, 2014, **4**, 4254–4260.
43 H. Q. Xu, J. Hu, D. Wang, Z. Li, Q. Zhang, Y. Luo, S. H. Yu and H. L. Jiang, *J. Am. Chem. Soc.*, 2015, **137**, 13440–13443.
44 S. Ali Akbar Razavi and A. Morsali, *Coord. Chem. Rev.*, 2019, **399**, 213023.
45 J. Liang, H. Yu, J. Shi, B. Li, L. Wu and M. Wang, *Adv. Mater.*, 2023, **35**, 2209814.
46 X. J. Kong, T. He, J. Zhou, C. Zhao, T. C. Li, X. Q. Wu, K. Wang and J. R. Li, *Small*, 2021, **17**, 2005357.
47 Y. Fu, X. Zhu, L. Huang, X. Zhang, F. Zhang and W. Zhu, *Appl. Catal., B*, 2018, **239**, 46–51.
48 Y. Fu, D. Sun, Y. Chen, R. Huang, Z. Ding, X. Fu and Z. Li, *Angew. Chem., Int. Ed.*, 2012, **51**, 3364–3367.
49 S. Lin, P. M. Usov and A. J. Morris, *Chem. Commun.*, 2018, **54**, 6965–6974.
50 T. Zhang and W. Lin, *Chem. Soc. Rev.*, 2014, **43**, 5982.
51 K. Merkel, J. Greiner and F. Ortmann, *Sci. Rep.*, 2023, **13**, 1685.
52 D. H. Streater, E. R. Kennehan, D. Wang, C. Fiankor, L. Chen, C. Yang, B. Li, D. Liu, F. Ibrahim, I. Hermans, K. L. Kohlstedt, L. Luo, J. Zhang and J. Huang, *J. Am. Chem. Soc.*, 2024, **146**, 4489–4499.
53 K. Song, S. Liang, X. Zhong, M. Wang, X. Mo, X. Lei and Z. Lin, *Appl. Catal., B*, 2022, **309**, 121232.
54 J. Lin, W. Tian, H. Zhang, X. Duan, H. Sun and S. Wang, *Energy Fuels*, 2021, **35**, 7–24.
55 L. Schumacher and R. Marschall, *Top. Curr. Chem.*, 2022, **380**, 53.
56 H. Sudrajat, H. Sudrajat, H. Sudrajat and M. Nobatova, *RSC Appl. Interfaces*, 2025, **2**, 599–619.

57 Q. Wang, J. Lian, Y. Bai, J. Hui, J. Zhong, J. Li, N. An, J. Yu and F. Wang, *Mater. Sci. Semicond. Process.*, 2015, **40**, 418–423.

58 Y. Han, H. Xu, Y. Su, Z. Liang Xu, K. Wang and W. Wang, *J. Catal.*, 2019, **370**, 70–78.

59 Y. C. Hao, L. W. Chen, J. Li, Y. Guo, X. Su, M. Shu, Q. Zhang, W. Y. Gao, S. Li, Z. L. Yu, L. Gu, X. Feng, A. X. Yin, R. Si, Y. W. Zhang, B. Wang and C. H. Yan, *Nat. Commun.*, 2021, **12**, 2682.

60 W. Zhong, R. Sa, L. Li, Y. He, L. Li, J. Bi, Z. Zhuang, Y. Yu and Z. Zou, *J. Am. Chem. Soc.*, 2019, **141**, 7615–7621.

61 M. Eddaoudi, H. Li and O. M. Yaghi, *J. Am. Chem. Soc.*, 2000, **122**, 1391–1397.

62 A. Dhakshinamoorthy, Z. Li and H. Garcia, *Chem. Soc. Rev.*, 2018, **47**, 8134–8172.

63 J. Lee, O. K. Farha, J. Roberts, K. A. Scheidt, S. T. Nguyen and J. T. Hupp, *Chem. Soc. Rev.*, 2009, **38**, 1450–1459.

64 M. Alvaro, E. Carbonell, B. Ferrer, F. X. Llabrés, I. Xamena and H. Garcia, *Chem. – Eur. J.*, 2007, **13**, 5106–5112.

65 D. Chen, Z. Guo, B. Li and H. Xing, *New J. Chem.*, 2022, **46**, 16297–16302.

66 M. Zhang, D. Zhang, X. Jing, B. Xu and C. Duan, *Angew. Chem., Int. Ed.*, 2024, **63**, e202402755.

67 K. Sun, Y. Huang, Q. Wang, W. Zhao, X. Zheng, J. Jiang and H. L. Jiang, *J. Am. Chem. Soc.*, 2024, **146**, 3241–3249.

68 X. M. Cheng, X. Y. Dao, S. Q. Wang, J. Zhao and W. Y. Sun, *ACS Catal.*, 2021, **11**, 650–658.

69 W. Xu, G. R. Zhang, J. Wang, H. Yu, W. Zhang, L. L. Shen and D. Mei, *Adv. Funct. Mater.*, 2023, **34**(9), 2312691.

70 Y. L. Dong, Y. Jiang, S. Ni, G. W. Guan, S. T. Zheng, Q. Guan, L. M. Pei and Q. Y. Yang, *Small*, 2023, **20**(23), 2308005.

71 L. Wang, P. Jin, S. Duan, H. She, J. Huang and Q. Wang, *Sci. Bull.*, 2019, **64**, 926–933.

72 L. Wang, J. Mao, G. Huang, Y. Zhang, J. Huang, H. She, C. Liu, H. Liu and Q. Wang, *Chem. Eng. J.*, 2022, **446**, 137011.

73 W. W. Dong, J. Jia, Y. Wang, J. R. An, O. Y. Yang, X. J. Gao, Y. L. Liu, J. Zhao and D. S. Li, *Chem. Eng. J.*, 2022, **438**, 135622.

74 S. Xie, C. Deng, Q. Huang, C. Zhang, C. Chen, J. Zhao and H. Sheng, *Angew. Chem., Int. Ed.*, 2023, **62**, e202216717.

75 H. Jiang, L. Wang, X. Yu, L. Sun, J. Li, J. Yang and Q. Liu, *Chem. Eng. J.*, 2023, **466**, 143129.

76 D. Lan, D. Yongping, B. Fenghua, C. Gonglai, Z. Shuwei, Y. Xiaoxue, L. Huiqin and W. Xiaojing, *Inorg. Chem.*, 2023, **62**, 2289–2303.

77 S. Karmakar, S. Barman, F. A. Rahimi, D. Rambabu, S. Nath and T. K. Maji, *Nat. Commun.*, 2023, **14**, 4508.

78 N. Y. Huang, H. He, S. Liu, H. L. Zhu, Y. J. Li, J. Xu, J. R. Huang, X. Wang, P. Q. Liao and X. M. Chen, *J. Am. Chem. Soc.*, 2021, **143**, 17424–17430.

79 H. Wu, X. Y. Kong, X. Wen, S. P. Chai, E. C. Lovell, J. Tang and Y. H. Ng, *Angew. Chem., Int. Ed.*, 2021, **60**, 8455–8459.

80 S. Karmakar, S. Barman, F. A. Rahimi and T. K. Maji, *Energy Environ. Sci.*, 2021, **14**, 2429–2440.

81 J. Li, H. Huang, W. Xue, K. Sun, X. Song, C. Wu, L. Nie, Y. Li, C. Liu, Y. Pan, H. L. Jiang, D. Mei and C. Zhong, *Nat. Catal.*, 2021, **4**, 719–729.

82 H. Ma, T. Wang, Y. Xu, W. Shi, R. Ma, Z. Xia, Q. Yang, G. Xie and S. Chen, *Appl. Catal., B*, 2024, **349**, 123857.

83 D. Liu, J. Hua, W. Zhang, K. Wei, S. Song, Q. Wang, Z. Song, H. Han, C. Ma and S. Feng, *Colloids Surf., A*, 2024, **695**, 134101.

84 K. Yuan, K. Tao, T. Song, Y. Zhang, T. Zhang, F. Wang, S. Duan, Z. Chen, L. Li, X. Zhang, D. Zhong, Z. Tang, T. B. Lu and W. Hu, *J. Am. Chem. Soc.*, 2024, **146**, 6893–6904.

85 C. Han, X. Zhang, S. Huang, Y. Hu, Z. Yang, T. T. Li, Q. Li and J. Qian, *Adv. Sci.*, 2023, **10**, 2300797.

86 Y. Su, Z. Song, W. Zhu, Q. Mu, X. Yuan, Y. Lian, H. Cheng, Z. Deng, M. Chen, W. Yin and Y. Peng, *ACS Catal.*, 2021, **11**, 345–354.

87 H. Zhang, T. Wang, J. Wang, H. Liu, T. D. Dao, M. Li, G. Liu, X. Meng, K. Chang, L. Shi, T. Nagao and J. Ye, *Adv. Mater.*, 2016, **28**, 3703–3710.

88 S. Wang, B. Y. Guan, Y. Lu and X. W. Lou, *J. Am. Chem. Soc.*, 2017, **139**, 17305–17308.

89 S. Wang, B. Y. Guan and X. W. D. Lou, *J. Am. Chem. Soc.*, 2018, **140**, 5037–5040.

90 T. Wang, L. Shi, J. Tang, V. Malgras, S. Asahina, G. Liu, H. Zhang, X. Meng, K. Chang, J. He, O. Terasaki, Y. Yamauchi and J. Ye, *Nanoscale*, 2016, **8**, 6712–6720.

91 S. Zhao, K. Li, J. Wu, J. Zhang, X. Li, X. Guo and C. Song, *ACS Appl. Mater. Interfaces*, 2022, **14**, 20375–20384.

92 J. Sun, X. Li, J. Li, M. Mu and X. Yin, *Colloids Surf., A*, 2022, **653**, 129940.

93 Y. Wang, J. Xu, J. Wan, J. Wang and L. Wang, *J. Colloid Interface Sci.*, 2022, **616**, 532–538.

94 Y. Xiao, Q. Zhang, L. Yang, Q. Zhang, X. Fu, L. Cheng and Q. Zeng, *Sep. Purif. Technol.*, 2023, **311**, 123172.

95 Y. Wang, W. Qian, G. Zhou, S. Zhang, X. Zhu, L. Li, X. Zhu, X. Wang, X. Han and J. Yi, *Chem. Eng. J.*, 2024, **501**, 157513.

96 X. H. Chen, Y. S. Zhang, W. Bin Li, X. W. Guan, J. W. Ye, L. Chen, H. P. Wang, J. Bai, Z. W. Mo and X. M. Chen, *Inorg. Chem. Front.*, 2022, **9**, 2328–2335.

97 G. Zhou, B. Wang and R. Cao, *J. Am. Chem. Soc.*, 2020, **142**, 14848–14853.

98 Z. Liang, H. Y. Wang, H. Zheng, W. Zhang and R. Cao, *Chem. Soc. Rev.*, 2021, **50**, 2540–2581.

99 A. M. May and J. L. Dempsey, *Chem. Sci.*, 2024, **15**, 6661–6678.

100 S. Mandal, S. Natarajan, P. Mani and A. Pankajakshan, *Adv. Funct. Mater.*, 2021, **31**, 2006291.

101 W. S. Cheon, J. Bu, S. Jung, J. Y. Yang, S. Choi, J. Kim, J. H. Baek, S. Park, M. K. Lee, S. E. Jun, S. H. Park, H. Park, S. A. Lee, S. H. Cho, M. Shokouhimehr, M. Senna and H. W. Jang, *Chem. Eng. J.*, 2024, **489**, 151004.

102 E. Kecsenovity, B. Endrödi, P. S. Tóth, Y. Zou, R. A. W. Dryfe, K. Rajeshwar and C. Janáky, *J. Am. Chem. Soc.*, 2017, **139**, 6682–6692.

103 M. Schreier, J. Luo, P. Gao, T. Moehl, M. T. Mayer and M. Grätzel, *J. Am. Chem. Soc.*, 2016, **138**, 1938–1946.

104 C. Y. Toe, Z. Zheng, H. Wu, J. Scott, R. Amal and Y. H. Ng, *Angew. Chem.*, 2018, **130**, 13801–13805.

105 M. Duan, C. Hu, H. Li, Y. Chen, R. Chen, W. Gong, Z. Lu, N. Zhang, R. Long, L. Song and Y. Xiong, *JACS Au*, 2022, **2**, 1160–1168.

106 P. Li, X. Lu, Z. Wu, Y. Wu, R. Malpass-Evans, N. B. McKeown, X. Sun and H. Wang, *Angew. Chem., Int. Ed.*, 2020, **59**, 10918–10923.

107 X. Lu, Z. Jiang, X. Yuan, Y. Wu, R. Malpass-Evans, Y. Zhong, Y. Liang, N. B. McKeown and H. Wang, *Sci. Bull.*, 2019, **64**, 1890–1895.

108 Y. Ma, X. Yi, S. Wang, T. Li, B. Tan, C. Chen, T. Majima, E. R. Waclawik, H. Zhu and J. Wang, *Nat. Commun.*, 2022, **13**, 1400.

109 Y. Shu, X. Liu, M. Zhang, B. Liu and Z. Wang, *Appl. Catal., B*, 2024, **346**, 123746.

110 R. Das, S. Chakraborty and S. C. Peter, *ACS Energy Lett.*, 2021, **6**(9), 3270–3274.

111 G. Liao, G. Ding, B. Yang and C. Li, *Precis. Chem.*, 2024, **2**(2), 49–56.

112 Y. Zhang, L. Cao, G. Bai and X. Lan, *Small*, 2023, **19**, 2300035.

113 M. Zhou, Z. Wang, A. Mei, Z. Yang, W. Chen, S. Ou, S. Wang, K. Chen, P. Reiss, K. Qi, J. Ma and Y. Liu, *Nat. Commun.*, 2023, **14**, 2473.

114 S. Gao, Q. Zhang, X. Su, X. Wu, X. G. Zhang, Y. Guo, Z. Li, J. Wei, H. Wang, S. Zhang and J. Wang, *J. Am. Chem. Soc.*, 2023, **145**, 9520–9529.

115 J. Wang, W. Zhu, F. Meng, G. Bai, Q. Zhang and X. Lan, *ACS Catal.*, 2023, **13**, 4316–4329.

116 J. Zhou, J. Li, L. Kan, L. Zhang, Q. Huang, Y. Yan, Y. Chen, J. Liu, S. L. Li and Y. Q. Lan, *Nat. Commun.*, 2022, **13**, 4681.

117 M. Kou, W. Liu, Y. Wang, J. Huang, Y. Chen, Y. Zhou, Y. Chen, M. Ma, K. Lei, H. Xie, P. K. Wong and L. Ye, *Appl. Catal., B*, 2021, **291**, 120146.

118 Y. N. Gong, W. Zhong, Y. Li, Y. Qiu, L. Zheng, J. Jiang and H. L. Jiang, *J. Am. Chem. Soc.*, 2020, **142**, 16723–16731.

119 W. Liu, X. Li, C. Wang, H. Pan, W. Liu, K. Wang, Q. Zeng, R. Wang and J. Jiang, *J. Am. Chem. Soc.*, 2019, **141**, 17431–17440.

120 M. Lu, J. Liu, Q. Li, M. Zhang, M. Liu, J. Wang, D. Yuan and Y. Lan, *Angew. Chem.*, 2019, **131**, 12522–12527.

121 M. Lu, Q. Li, J. Liu, F. M. Zhang, L. Zhang, J. L. Wang, Z. H. Kang and Y. Q. Lan, *Appl. Catal., B*, 2019, **254**, 624–633.

122 S. Guo, H. Zhang, Y. Chen, Z. Liu, B. Yu, Y. Zhao, Z. Yang, B. Han and Z. Liu, *ACS Catal.*, 2018, **8**, 4576–4581.

123 R. Xu, X. S. Wang, H. Zhao, H. Lin, Y. B. Huang and R. Cao, *Catal. Sci. Technol.*, 2018, **8**, 2224–2230.

124 S. Yang, W. Hu, X. Zhang, P. He, B. Pattengale, C. Liu, M. Cendejas, I. Hermans, X. Zhang, J. Zhang and J. Huang, *J. Am. Chem. Soc.*, 2018, **140**, 14614–14618.
125 P. Fu, C. Chen, C. Wu, B. Meng, Q. Yue, T. Chen, W. Yin, X. Chi, X. Yu, R. Li, Y. Wang, Y. Zhang, W. Luo, X. Liu, Y. Han, J. Wang, S. Xi and Y. Zhou, *Angew. Chem., Int. Ed.*, 2025, **64**, e202415202.
126 Y. Xu, J. P. Dong, L. Wang, R. L. Geng, R. Wang, Y. N. Si, S. Q. Zang and T. C. W. Mak, *Angew. Chem., Int. Ed.*, 2025, **64**, e202501391.
127 W. Lin, F. Lin, J. Lin, Z. Xiao, D. Yuan and Y. Wang, *J. Am. Chem. Soc.*, 2024, **146**, 16229–16236.
128 Z. X. Pan, S. Yang, X. Chen, J. X. Luo, R. Z. Zhang, P. Yang, Q. Xu and J. Y. Yue, *Chem. Eng. J.*, 2024, **493**, 152798.
129 S. Yang, R. Sa, H. Zhong, H. Lv, D. Yuan and R. Wang, *Adv. Funct. Mater.*, 2022, **32**, 2110694.
130 Y. Zhang, Y. Liu, H. Li, G. Bai and X. Lan, *Chem. Eng. J.*, 2024, **489**, 151479.
131 R. K. Yadav, A. Kumar, N. J. Park, K. J. Kong and J. O. Baeg, *J. Mater. Chem. A*, 2016, **4**, 9413–9418.
132 K. Guo, X. Zhu, L. Peng, Y. Fu, R. Ma, X. Lu, F. Zhang, W. Zhu and M. Fan, *Chem. Eng. J.*, 2021, **405**, 127011.
133 Z. Fan, Y. Cai, Z. Yang, X. Zhang, R. Shao, S. Zhong, L. Zhao, D. Liu and S. Bai, *Appl. Catal., B*, 2024, **351**, 123979.
134 Y. Liu, Y. Wang, J. Shang, J. Peng and T. Zhu, *Appl. Catal., B*, 2024, **350**, 123937.
135 Y. Yang, H. Y. Zhang, Y. Wang, L. H. Shao, L. Fang, H. Dong, M. Lu, L. Z. Dong, Y. Q. Lan and F. M. Zhang, *Adv. Mater.*, 2023, **35**, 2304170.
136 X. Yang, X. Lan, Y. Zhang, H. Li and G. Bai, *Appl. Catal., B*, 2023, **325**, 122393.
137 L. Zou, R. Sa, H. Zhong, H. Lv, X. Wang and R. Wang, *ACS Catal.*, 2022, **12**, 3550–3557.
138 M. Zhang, M. Lu, Z. Lang, J. Liu, M. Liu, J. Chang, L. Li, L. Shang, M. Wang, S. Li and Y. Lan, *Angew. Chem.*, 2020, **132**, 6562–6568.
139 J. C. Soc and C. Commun, *J. Chem. Soc., Chem. Commun.*, 1983, 536–538.
140 H. Takeda, K. Koike, H. Inoue and O. Ishitani, *J. Am. Chem. Soc.*, 2008, **130**, 2023–2031.
141 S. A. Lee, J. Bu, J. Lee and H. W. Jang, *Small Sci.*, 2023, **3**, 2200109.
142 W. S. Cheon, S. G. Ji, J. Kim, S. Choi, J. W. Yang, S. E. Jun, C. Kim, J. Bu, S. Park, T. H. Lee, J. Wang, J. Y. Kim, S. A. Lee, J. Y. Kim and H. W. Jang, *EES Catal.*, 2025, **3**, 140–151.
143 Y. N. Gong, J. H. Mei, W. J. Shi, J. W. Liu, D. C. Zhong and T. B. Lu, *Angew. Chem., Int. Ed.*, 2024, **63**, e202318735.